Journal of Computational Physics 228 (2009) 6016–6036

Contents lists available at ScienceDirect

Journal of Computational Physics

journal homepage: www.elsevier.com/locate/jcp

A domain decomposition method for two-phase transport model in the cathode of a polymer electrolyte fuel cell

Pengtao Sun [a,*], Guangri Xue [b,1], Chao-yang Wang [c], Jinchao Xu [b,d]

[a] Department of Mathematical Sciences, University of Nevada, Las Vegas, 4505 Maryland Parkway, Las Vegas, NV 89154, USA
[b] Department of Mathematics, The Pennsylvania State University, University Park, PA 16802, USA
[c] Department of Mechanical and Nuclear Engineering, Electrochemical Engine Center (ECEC), The Pennsylvania State University, University Park, PA 16802, USA
[d] Laboratory of Mathematics and Applied Mathematics, School of Mathematical Sciences, Peking University, Beijing 100871, China

ARTICLE INFO

Article history:
Received 1 December 2007
Received in revised form 4 March 2009
Accepted 9 May 2009
Available online 18 May 2009

Keywords:
Two-phase model
Polymer electrolyte fuel cell
Kirchhoff transformation
Domain decomposition
Dirichlet–Neumann alternating iteration
Combined finite element-upwind finite volume method

ABSTRACT

Using *Kirchhoff* transformation, we develop a *Dirichlet–Neumann* alternating iterative domain decomposition method for a 2D steady-state two-phase model for the cathode of a polymer electrolyte fuel cell (PEFC) which contains a channel and a gas diffusion layer (GDL). This two-phase PEFC model is represented by a nonlinear coupled system which typically includes a modified *Navier–Stokes* equation with Darcy's drag as an additional source term of the momentum equation, and a convection–diffusion equation for the water concentration with discontinuous and degenerate diffusivity. For both cases of dry and wet gas channel, we employ *Kirchhoff* transformation and *Dirichlet–Neumann* alternating iteration with appropriate interfacial conditions on the GDL/channel interface to treat the jump nonlinearities in the water equation. Numerical experiments demonstrate that fast convergence as well as accurate numerical solutions are obtained simultaneously owing to the implementation of the above-described numerical techniques along with a combined finite element-upwind finite volume discretization to automatically control the dominant convection terms arising in the gas channel.

1. Introduction

Water management is critical to achieving high performance of polymer electrolyte fuel cells (PEFC). The polymer electrolyte membrane requires sufficient water to exhibit a high ionic conductivity. During fuel cell operation, water molecules migrate through the membrane under electro-osmotic drag, hydraulic permeation, and molecular diffusion, making it difficult to retain a high water content within the membrane. Generally, humidification is applied to the inlet gases of the anode and/or cathode in order to keep the membrane hydrated. On the other hand, water is generated in the cathode due to the electrochemical reaction of H^+/O_2. If the water generated is not removed from the cathode at a sufficient rate, cathode flooding may result and the oxygen gas transport is hindered. Thus, a relatively dry air at the cathode inlet is sometimes helpful to remove excessive water.

The importance of two-phase transport in a PEFC has been stressed in Ref. [32,33]. During fuel cell operation, especially at high current densities, liquid water is likely to appear in the cathode, resulting in two-phase transport phenomena. The transport processes then become significantly more complicated due to the coupled flow of liquid water and gaseous reactants in porous media [31,4]. Wang et al. [44,45] studied the gas–liquid, two-phase flow and transport in the air cathode of

* Corresponding author. Tel.: +1 702 895 5175; fax: +1 702 895 4343.
E-mail addresses: pengtao.sun@unlv.edu (P. Sun), gxue@ices.utexas.edu (G. Xue), cxw31@psu.edu (C.-y. Wang), xu@math.psu.edu (J. Xu).
[1] Present address: Institute for Computational Engineering and Sciences (ICES), The University of Texas at Austin, Austin, TX 78712, USA.

0021-9991/$ - see front matter © 2009 Elsevier Inc. All rights reserved.
doi:10.1016/j.jcp.2009.05.008

PEFCs including hydrogen and direct methanol fuel cells, and discussed single-and two-phase transport regimes based on the multiphase mixture model previously developed by Wang [43] for two-phase flow and multicomponent transport in porous media. Pasaogullari and Wang [25] presented a predictive capability for flooding in multidimensional, full PEFC with realistic hydrophobic GDL, and described a two-phase, multidimensional PEFC model to investigate the effects of two-phase transport and flooding on PEFC performance, particularly the effects of the flow rate (i.e. the flow stoichiometry) and the inlet humidity. This two-phase PEFC model is represented by a nonlinear coupled system for velocity and concentration fields, which typically includes a modified *Navier–Stokes* equation with Darcy's drag as an additional source term of the momentum equation, and a convection–diffusion equation for water concentration.

However, the water transport equation in this two-phase PEFC model may feature a discontinuous and degenerate diffusivity, especially in the case of dry gas channels (see (2.6) and Fig. 2.1). For standard finite element or finite volume methods combining with standard *Picard*'s iteration, which are carried out in Ref. [25] and are also generally employed in commercial fluid solvers, the significant discontinuity and degeneracy of the diffusion coefficient introduces oscillating nonlinear iterations to the water transport equation, and make the standard numerical approaches fail to attain convergent nonlinear iterations [36]. The dominant convection coefficient is another difficulty in obtaining stable and convergent iteration for *Navier–Stokes* equation and convection–diffusion equation in gas channels.

Therefore, to obtain physically reasonable solutions, mass balance errors are usually checked instead of the convergence criteria of numerical schemes. However, in the sense of numerical approximation, mass balance is only the necessary condition of a convergent numerical iteration, not the sufficient condition. For robust and efficient numerical solutions, we need to design new numerical approaches and achieve truly convergent numerical iterations.

The main purpose of this paper is to develop new numerical techniques for the steady-state two-phase model of PEFCs, as presented in Ref. [25], for both cases of a dry and a wet gas channel. In this model much of the difficulty lies in how to efficiently deal with the discontinuous and degenerate diffusivity arising in the water concentration equation.

We employ *Kirchhoff* transformation [37,9,1,7,2,29,46] to specifically handle the discontinuous and degenerate diffusivity arising in the two-phase transport model of a PEFC with the intention to accelerate the nonlinear iteration and obtain accurate solution. We have successfully dealt with this problem in the case of dry channel in terms of *Kirchhoff* transformation for two-phase PEFC model [37]. However, when the gas channel turns out to be wet, the diffusivity of water concentration equation is discontinuous across the interface of GDL and gas channel. Thus the new variable after introducing *Kirchhoff* transformation becomes discontinuous as well, which makes the numerical solution incorrect. To overcome this problem, in this paper we present *Dirichlet–Neumann* alternating iterative domain decomposition method [6,27] to solve the reformulated two-phase PEFC model derived from *Kirchhoff* transformation, and recover the accurate numerical solution as well as fast nonlinear iteration. On the other hand, *Dirichlet–Neumann* alternating iterative domain decomposition method can also work for the case of dry gas channel as well. Hence, this method covers both cases.

The rest of this paper is organized as follows. First, we introduce the governing equations for the steady-state two-phase transport problem in both gas channel and GDL in Section 2. In Section 3, we describe the reformulated water concentration equation using *Kirchhoff* transformation and address how efficiently it deals with the discontinuous and degenerate diffusivity. The *Dirichlet–Neumann* alternating iterative domain decomposition method will be introduced in Section 4. In order to efficiently control the dominant convection terms arising in the gas channel due to the large velocity therein, we introduce a combined finite element-upwind finite volume method [11,13,12] in Section 5, where we specifically discretize the convection term with the upwind finite volume scheme, and simultaneously, apply finite element discretization to the remaining terms. The entire combined finite element-upwind finite volume discretizations are given in Section 6, where we basically employ mixed finite element method to discretize the momentum and continuity equations, solve an equivalent semilinear convection–diffusion equation with simple *Laplacian* term as diffusion for the original water concentration equation via *Dirichlet–Neumann* alternating iteration method, and apply upwind finite volume scheme to the dominant convection terms. Numerical experiments with a practical set of boundary conditions are given in Section 7 for both cases of a dry and a wet gas channel, demonstrating that our numerical schemes significantly improve the efficiency and accuracy of computational performance. On the other hand, the similar numerical results with [37] are also obtained here for the case of a dry gas channel,

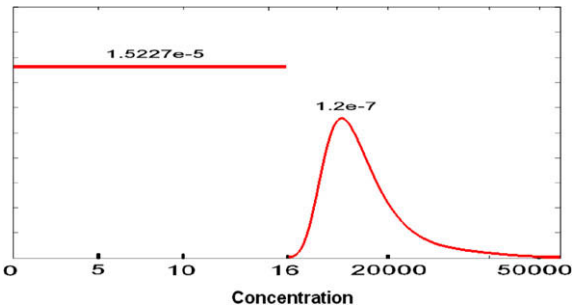

Fig. 2.1. $\Gamma(C)$.

indicating that *Dirichlet–Neumann* alternating iteration method can solve the case of a dry gas channel, simultaneously, despite that it is specifically designed for the case of wet gas channel.

2. Steady-state two-phase transport model in PEFC cathode

Based on [25], in this section we describe the governing equations for 2D steady-state two-phase transport problem in the cathode of PEFC, and define the relevant physical parameters and coefficients as well as their boundary conditions. All of the involved parameters are listed in Table 2.1 in Section 2.2.

2.1. Governing equations

We introduce the governing equations for flow and species concentration fields. These nonlinear equations are strongly coupled via velocity $\vec{u}$ and concentration C.

Flow equations. For flow field with velocity $\vec{u}$ and pressure P as unknowns, we have the following modified *Navier–Stokes* equations:

$$\begin{cases} \frac{1}{\varepsilon^2}\nabla\cdot(\rho\vec{u}\vec{u}) = \nabla\cdot(\mu\nabla\vec{u}) - \nabla P + S_u & (a) \\ \nabla\cdot(\rho\vec{u}) = 0 & (b) \end{cases} \tag{2.1}$$

where ρ is density and μ the effective viscosity, both functions of concentration C as defined in Section 2.2, and ε the porosity of air cathode. Here (2.1a) represents a modified momentum equation, in which the additional source term S_u physically represents Darcy's drag and is defined as follows:

$$S_u = -\frac{\mu}{K}\vec{u} \tag{2.2}$$

where K is a position-dependent permeability in a porous cathode, defined as

$$K = \begin{cases} +\infty & \text{in gas channel,} \\ K_{\mathrm{GDL}} = 10^{-12} & \text{in GDL,} \end{cases} \tag{2.3}$$

This definition of K implies that the gas channel is considered to be completely permeable, while GDL is described as a porous medium with small permeability K_{GDL}.

Darcy's drag S_u is developed from *Darcy*'s Law in a porous GDL:

$$\vec{u} = -\frac{K_{\mathrm{GDL}}}{\mu}\nabla P \tag{2.4}$$

when $K = \infty$ in gas channel, $S_u = 0$ according to (2.2). Therefore (2.1a) reduces identically to the classical momentum equation. On the other hand, in GDL (2.1a) becomes *Darcy*'s law because the permeability $K_{\mathrm{GDL}} = 10^{-12}$ is so small that all the remaining terms in (2.1a) become negligible, except for the pressure gradient vector which drives flow.

By virtue of this additional source term S_u, the momentum balance equation is valid in both GDL and gas channel, reducing to the *Darcy*'s law for two-phase flow in a porous GDL with a small permeability or the *Navier–Stokes* equation in a gas channel with the porosity being unity and the permeability being infinity. Note that $\vec{u}$ is the intrinsic velocity vector based on the open pore area only. (2.1) is also known as *Darcy–Brinkman–Forchheimer* model [18], which is typically used to model the flow inside coarse porous media. [8] employed finite-difference methods for such model involving the *Navier–Stokes* equations with an added Darcy term. Xie et al. [47] designed and analyzed uniformly stable finite element methods for the linear case of (2.1) with single phase flow and no convection term.

Table 2.1
Property parameters

Parameter	Symbol	Value	Unit
Water vapor diffusivity	D_{gas}	2.6×10^{-5}	m^2/s
Water molecular weight	M	0.018	kg/mol
Saturated water concentration	C_{sat}	16	mol/m^3
Vapor density	ρ_g	0.882	kg/m^3
Liquid water density	ρ_l	971.8	kg/m^3
Surface tension	σ	0.0625	kg/s^2
Contact angle between two-phases	θ_c	$\frac{2}{3}\pi$	
Porosity of GDL	ε	0.7	
Permeability of GDL	K_{GDL}	1.0×10^{-12}	m^2
Kinematic liquid water viscosity	ν_l	3.533×10^{-7}	m^2/s
Kinematic vapor viscosity	ν_g	3.59×10^{-5}	m^2/s
Faraday constant	F	96,487	A·s/mol
Current density at the left end	I_1	20,000	A/m^2
Current density at the right end	I_2	10,000	A/m^2

The advantage of the modified *Navier–Stokes* equations (2.1) is that we can simultaneously solve *Darcy–Navier–Stokes* flow in one single domain, instead of two-domain approach where *Beavers–Joseph–Saffman* interface condition [5,30,15] and continuity of mass flux and continuity of normal stress must be employed at the GDL/channel interface. Obviously the single domain approach is easier to implement, especially in simulation of three-dimensional complete fuel cell problems.

Species concentration equation. Due to the coexistence of a single-phase zone and a two-phase zone and the coupled flow of liquid water and gaseous reactants in porous media, the water conservation equation turns out to be the most important and difficult species equation to solve for fuel cell simulation. Therefore, for species concentration equations, in order to focus on the water management issue, without loss of generality, we consider a single component model by taking water as the only species in the simplified concentration equation.

The water concentration equation is given as follows [25]:

$$\begin{cases} \nabla\cdot(\gamma_c\vec{u}C) = \nabla\cdot(\Gamma(C)\nabla C), \text{ in GDL}, & (a)\\ \nabla\cdot(\vec{u}C) = \nabla\cdot(D_g^{eff}\nabla C), \text{ in gas channel}, & (b)\end{cases} \tag{2.5}$$

where γ_c is the advection correction factor defined in Section 2.2. The diffusivity $\Gamma(C)$ in GDL is defined as

$$\Gamma(C) = \begin{cases} \Gamma_{capdiff}, \text{ if } C \geqslant C_{\text{sat}};\\ D_g^{eff}, \text{ if } C < C_{\text{sat}}.\end{cases} \tag{2.6}$$

Here C_{sat} is the saturated water concentration, $D_g^{eff} = \varepsilon^{1.5}D_{gas}$ the effective water vapor diffusivity in the gas phase region, and $\Gamma_{capdiff}$ a capillary diffusion coefficient in the two-phase region, which is defined as a function of liquid saturation s:

$$\Gamma_{capdiff} = \left|\left(\frac{\text{mf}_l}{M} - \frac{C_{\text{sat}}}{\rho_g}\right)\left(\frac{M}{\rho_l - C_{\text{sat}}M}\right)\frac{\lambda_l\lambda_g}{\nu}\sigma\cos\theta_c(\varepsilon K)^{1/2}\frac{dJ(s)}{ds}\right| \tag{2.7}$$

Here $s\in[0,1]$ denotes the liquid saturation throughout this paper, and is a fundamental variable in multiphase mixture (M^2) model [43,45], having coequality with water concentration as

$$C = \frac{\rho_l s}{M} + C_{\text{sat}}(1-s), \quad \text{hence} \quad s = (C - C_{\text{sat}})/\left(\frac{\rho_l}{M} - C_{\text{sat}}\right). \tag{2.8}$$

$J(s)$ is the *Leverett* function, given by the following relation [22,24,25]

$$J(s) = \begin{cases} 1.417(1-s) - 2.120(1-s)^2 + 1.263(1-s)^3, & \text{if } \theta_c < 90^\circ;\\ 1.417s - 2.120s^2 + 1.263s^3, & \text{if } \theta_c > 90^\circ.\end{cases}$$

So, despite the complicated definition $\Gamma_{capdiff}$ is a rational function of concentration C.

According to the definitions of physical parameters and coefficients in Section 2.2, one can easily see that $\Gamma_{capdiff} = 0$ when $C = C_{\text{sat}}$, or $s = 0$. So $\Gamma_{capdiff}$, and further $\Gamma(C)$, is degenerate at C_{sat}.

The behavior of diffusivity function $\Gamma(C)$ can be better understood in Fig. 2.1, where $\Gamma(C)$ is clearly indicated as a discontinuous and degenerate function with respect to C. $C_{\text{sat}} = 16$ mol/m^3 (for 80 °C) is the typical point at which discontinuity and degeneracy occur for $\Gamma(C)$ at the same time.

Governing Eqs. (2.1) and (2.5), together with the definitions of physical coefficients and parameters in Section 2.2 and the boundary conditions in Section 2.3, constitute a 2D steady-state two-phase transport model for the cathode of a polymer electrolyte fuel cell.

2.2. Coefficients and parameters

The physical coefficients and mixture variables arising in the governing Eqs. (2.1), (2.5) and the definitions of their coefficients are defined as follows:

- Density: $\rho = \rho_l s + \rho_g(1-s)$.
- Relative mobilities: $\lambda_l(s) = \frac{k_{rl}/\nu_l}{k_{rl}/\nu_l + k_{rg}/\nu_g}$, $\lambda_g(s) = 1 - \lambda_l(s)$.
- Relative permeabilities: $k_{rl} = s^3$, $k_{rg} = (1-s)^3$.
- Kinematic viscosity: $\nu = (\frac{k_{rl}}{\nu_l} + \frac{k_{rg}}{\nu_g})^{-1}$.
- Effective viscosity: $\mu = \frac{\rho_l\cdot s + \rho_g\cdot(1-s)}{\frac{k_{rl}}{\nu_l} + \frac{k_{rg}}{\nu_g}}$.
- Advection correction factor:

$$\gamma_c = \frac{\rho(\lambda_l \text{mf}_l + \lambda_g \text{mf}_g)}{\rho_l \text{mf}_l s + \rho_g \text{mf}_g(1-s)}, \tag{2.9}$$

where $\text{mf}_l = 1$ and $\text{mf}_g = \frac{C_{\text{sat}}M}{\rho_g}$ are mass fractions of liquid water and gaseous water, respectively. γ_c is a continuous function of concentration. In the gas channel we assume that water only exists in the gaseous phase, so $s = 0$, and the advection

correction factor γ_c defined above becomes unity, which guarantees the convection term in (2.5) is continuous across the GDL/channel interface and furthermore, continuous in the entire domain, specifically for a dry gas channel. However, if the gas channel is wet, neither diffusivity nor convection coefficient in (2.5) is continuous across the GDL/channel interface; though, the mass flux is always continuous. We will discuss this issue in Section 3.

Other property parameters are referred to Table 2.1.

2.3. Computational domain and boundary conditions

We specifically consider that governing Eqs. (2.1) and (2.5) take place in the cathode of a PEFC which consists of a gas diffusion layer and a gas channel, as schematically shown in Fig. 2.2. The horizontal x-axis represents the flow direction and the vertical y-axis points in the through-plane direction. The geometric sizes of this computational domain are marked in Fig. 2.2 as well, where the physical width of the GDL and gas channel are $\delta_{GDL} = 3 \times 10^{-4}$ m, $\delta_{CH} = 10^{-3}$ m, respectively, in comparison with the length in flow direction $l_{PEFC} = 7 \times 10^{-2}$ m. The large aspect ratio of the channel length to width, about 1:100, give rise to a thin film flow structure.

For the simplicity of notation, in Section 4 the GDL and gas channel are represented by Ω_1 and Ω_2, respectively. Thus $\Omega = \Omega_1 \cup \Omega_2$. At the inlet of the gas channel ($(\partial\Omega)_1$ in Fig. 2.2), constant flow rate and water concentration are specified. At the outlet ($(\partial\Omega)_3$ in Fig. 2.2), both velocity and concentration fields are assumed to be fully developed. Hence based on this computational domain, the boundary conditions are indicated as follows.

For flow field Eq. (2.1), the following boundary conditions hold with respect to velocity $\vec{u}$:

- $(\partial\Omega)_1$: at channel inlet, the horizontal component of velocity $u_x = u_{x-\text{inlet}}$ (m/s) and its vertical component $u_y = 0$, where $u_x|_{\text{inlet}}$ will be given as a parabolic-like function in (6.9), where u_{in} is employed to represent the maximum value of $u_x|_{\text{inlet}}$.
- $(\partial\Omega)_3$: at channel outlet, $(PI - \mu\nabla\vec{u}) \cdot \vec{n} = 0$
- $(\partial\Omega)_5$: at the bottom wall, $\vec{u} = 0$,
- $(\partial\Omega)_2$, $(\partial\Omega)_4$, $(\partial\Omega)_6$: at side and top walls, $\vec{u} = 0$.

For water concentration (2.5), the following boundary conditions hold with respect to concentration C:

- $(\partial\Omega)_1$: at channel inlet, $C = C_{\text{in}}(\text{mol/m}^3)$,
- $(\partial\Omega)_2$, $(\partial\Omega)_3$, $(\partial\Omega)_4$, $(\partial\Omega)_5$: at the bottom and side walls and channel outlet, $\nabla C \cdot \vec{n} = 0$,
- $(\partial\Omega)_6$: at the top wall, the liquid water mass flux condition is given by:

$$\Gamma(C)\nabla C\vec{n} - \gamma_c \vec{u} C \cdot \vec{n} = \frac{I(x)}{2F}, \tag{2.10}$$

where the Dirichlet boundary condition at $(\partial\Omega)_1$ is usually set as $C_{\text{in}} < C_{\text{sat}}$ to indicate the input of gaseous component in two-phase PEFC model. At the membrane/cathode surface ($(\partial\Omega)_6$), the nonhomogeneous Neumann boundary condition is given to simulate oxygen reduction reaction occurring in catalyst layer and generating liquid water mass flux [42], where $I(x)$ is the volumetric transfer current of the reaction (or transfer current density) defined by a linear function as follows:

$$I(x) = \left(I_1 - (I_1 - I_2)\frac{x}{l_{\text{PEFC}}}\right)\left[\frac{A}{m^2}\right] \tag{2.11}$$

where I_1, I_2 are prescribed in Table 2.1. Eq. (2.11) is an approximation of the current density distribution for our simplified two-phase PEFC model without solving for an electrochemical model. Considering the positive water flux boundary condition (2.10) on the top wall and zero source in (2.5), the total source is eventually positive for the entire domain.

To result in a wet gas channel, there are two operating conditions we may adjust. One is to reduce the gas inlet speed u_{in}, consequently decreasing the convection effect in the gas channel and allowing liquid water to reach the interface of porous GDL and open channel, forming liquid droplets. The other way for liquid water to appear on the GDL/channel interface is to

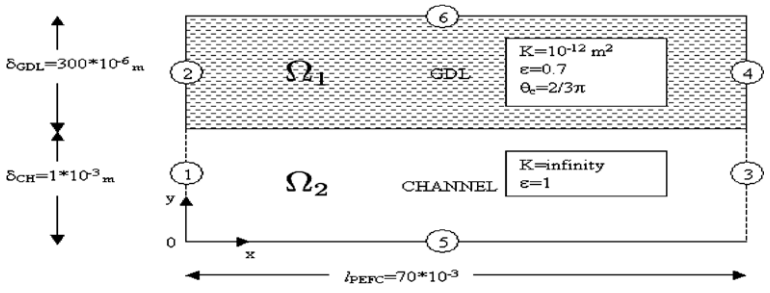

Fig. 2.2. Domain.

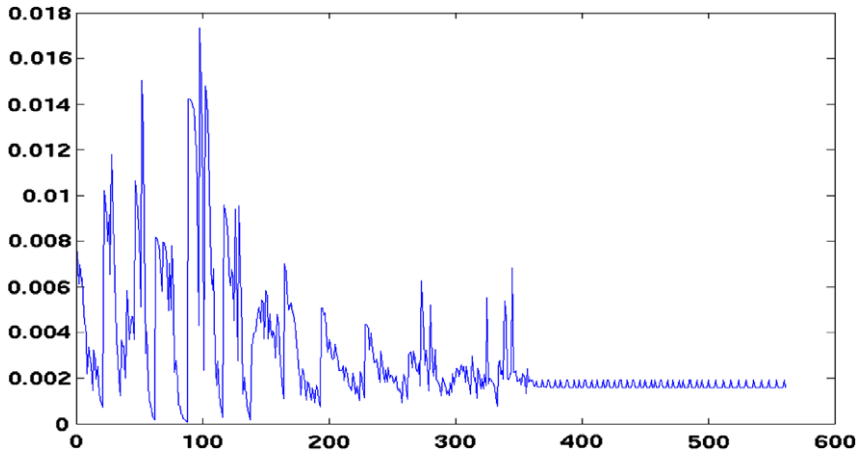

Fig. 2.3. Iteration history with standard finite element method and Picard's iteration for (2.5).

increase the current density $I(x)$ on the membrane/cathode surface; with more water generated from the oxygen reduction reaction, a wet gas channel results. Therefore, in our numerical experiments later in Section 7, we will simulate these two different cases of wetted gas channel with smaller inlet velocity u_{in} and larger current densities I_1, I_2, respectively.

So far we addressed 2D steady-state two-phase transport model (2.1), (2.5) in the cathode of a PEFC for water component only, and appropriately present flux boundary condition to simulate the chemical reaction taking place at the membrane/cathode interface. In summary, this model consists of highly nonlinear transport equations with discontinuous and degenerate diffusion in GDL as well as dominant convection in the gas channel, thus leading to numerical instabilities in nonlinear iteration, as shown in Fig. 2.3. This iteration history is obtained by standard linear finite element method with *Picard*'s iteration. In the following sections we will study and present new numerical techniques to overcome these instabilities.

3. *Kirchhoff* transformation

An efficient discretization scheme to deal with the nonlinear discontinuous and degenerate diffusivity $\Gamma(C)$ is the key to make the entire nonlinear iteration converge quickly. To this end, using *Kirchhoff* transformation [9,1,7,2,29,46], we are able to reformulate (2.5) into a semilinear convection–diffusion equation with simple *Laplacian* term as diffusion with respect to a new variable, where the nonlinearity, discontinuity and degeneracy arising in diffusivity $\Gamma(C)$ all disappear. Instead, we need to implicitly solve inverse *Kirchhoff* transformation in order to obtain the desired water concentration.

We define a new variable W in terms of *Kirchhoff* transformation

$$W(C) = \int_0^C \Gamma(\omega)\, d\omega. \tag{3.1}$$

Hence W is a function of concentration C, there exists no explicit expression for inverse *Kirchhoff* transformation (3.1), so a method needs to be found to compute C from W.

Notice however that for the water concentration equation in a dry channel (2.5b) with a constant diffusivity D_g^{eff}, we have the specific *Kirchhoff* transformation as follows

$$W = \int_0^C D_g^{\text{eff}}\, d\omega = D_g^{\text{eff}} C, \tag{3.2}$$

where *Kirchhoff*'s variable W is a linear function of C in gas channel, or inversely,

$$C = (D_g^{\text{eff}})^{-1} W. \tag{3.3}$$

Thus the full *Kirchhoff* transformation for diffusivity $\Gamma(C)$ in water concentration Eq. (2.5) is given as follows:

$$W = \begin{cases} \int_0^C \Gamma(\omega) d\omega & \text{in GDL,} \\ D_g^{\text{eff}} C & \text{in Channel.} \end{cases} \tag{3.4}$$

Consequently we have the following gradient of W by differentiating both sides of (3.4) with respect to spatial variables

$$\nabla W = \begin{cases} \Gamma(C)\nabla C & \text{in GDL,} \\ D_g^{\text{eff}} \nabla C & \text{in Channel.} \end{cases} \tag{3.5}$$

Under certain operating conditions, two-phase flow appears in the cathode channel, i.e. the wet channel. This is especially under a small inlet velocity of air flow, then sequentially a slow convection. On the other hand, as a result of both the electrochemical reaction and the water transport across the membrane from the anode, higher cell current density may give birth to more liquid water at membrane/cathode surface and result in the expansion of two-phase zone. Thus, its evaporation front propagates towards the GDL/channel interface, and eventually liquid water may come into the gas channel.

In this paper we specifically look at the case of a wet gas channel and attempt to develop an efficient numerical method for this case, moreover, the method should also be able to cover the case of a dry gas channel.

In view of Eq. (2.5), the diffusivity in the gas channel remains constant D_g^{eff}, while the diffusivity $\Gamma(C)$ in the two-phase zone of GDL is less than D_g^{eff} (see Fig. 2.1). Therefore the diffusivity of (2.5) is discontinuous across the GDL/channel interface. Further, according to (3.4), the resulted *Kirchhoff*'s variable W is discontinuous as well at the interface of GDL and channel.

However, concentration C is always continuous everywhere in the fuel cell, including at the GDL/channel interface, so is the mass flux of (2.5) such that

$$(\Gamma(C)\nabla C - \gamma_c \vec{u} C)\cdot \overrightarrow{n_2} = (D_g^{eff}\nabla C - \vec{u} C)\cdot \overrightarrow{n_2} \quad \text{at GDL/gas channel interface}, \tag{3.6}$$

where $\overrightarrow{n_2}$ is the outer normal vector pointing to GDL (Ω_1) from the gas channel (Ω_2) across the interface.

In the following we still reformulate (2.5) with *Kirchhoff* transformation (3.4) and properly impose the interfacial conditions on the GDL/channel interface as mentioned above. By virtue of (3.4) and (3.5), and considering continuity Eq. (2.1b) in the gas channel, we can reformulate (2.5) to be an equivalent water concentration equation system with respect to *Kirchhoff*'s variable W, along with corresponding interfacial and outer boundary conditions, namely:

$$\begin{cases} \Delta W_1 = \nabla\cdot(\gamma_c \vec{u} C_1) \quad \text{in } \Omega_1 & (a)\\ -\Delta W_2 + \nabla\cdot((D_g^{eff})^{-1}\vec{u} W_2) = 0 \quad \text{in } \Omega_2 & (b)\\ C_1 = C_2, \quad \text{on } \Sigma & (c)\\ (\nabla W_2 - (D_g^{eff})^{-1}\vec{u} W_2)\cdot\overrightarrow{n_2} = -(\nabla W_1 - \gamma_c C_1 \vec{u})\cdot\overrightarrow{n_1} \quad \text{on } \Sigma & (d)\\ W_2 = W_{\text{in}} \quad \text{on } (\partial\Omega)_1 & (e)\\ \frac{\partial W_1}{\partial n} - \gamma_c \vec{u} C_1\cdot\vec{n} = \frac{I}{2F} \quad \text{on } (\partial\Omega)_6 & (f)\\ \frac{\partial W_1}{\partial n} = \frac{\partial W_2}{\partial n} = 0 \quad \text{elsewhere on } \partial\Omega & (g) \end{cases} \tag{3.7}$$

where $\overrightarrow{n_i}(i=1,2)$ is the outer normal vector of Ω_i across Σ. Hereinafter, we employ notation Σ to denote the interface of GDL and gas channel. Obviously $\overrightarrow{n_2} = -\overrightarrow{n_1}$. $W_i, C_i (i = 1,2)$ denote the restriction of W and C in Ω_1 and Ω_2, respectively. $\vec{u}$ is known velocity which is derived from (2.1). W_{in} is the boundary value of W at channel inlet and is defined as $W_{\text{in}} = D_g^{eff} C_{\text{in}}$, according to the Dirichlet boundary condition of concentration C at inlet and (3.2).

We observe that only one Laplacian term is involved on the left hand side of (3.7a) and (3.7b), with the original discontinuous and degenerate diffusivity $\Gamma(C)$ hidden inside the *Kirchhoff* transformation (3.1). This significantly reduces the difficulty of nonlinear iteration of the reformulated equation and makes fast convergence possible. Now the only nonlinearity remains on the right hand side of (3.7a), i.e. the convection term $\nabla\cdot(\gamma_c \vec{u} C(W))$, where C is the implicit and nonlinear function of W in terms of inverse *Kirchhoff* transformation.

Indeed (3.7a) is only a semilinear equation because one single C stays on the right hand side which depends on W via inverse *Kirchhoff* transformation, an implicit function. *Picard*'s method is sufficient to linearize it. In each iteration step, C is updated by inverse *Kirchhoff* transformation from W. In contrast to (3.7a), (3.7b) is just a linear equation in the gas channel where velocity $\vec{u}$ is relatively large thus resulting in the dominant convection term in (3.7b). So we cannot treat this convection term as an additional source term but reformulate it into an explicit convection form of W via linear *Kirchhoff* transformation (3.3) and discretize it with upwind scheme to stabilize the numerical solution.

In view of the weak nonlinearity in (3.7), we expect fast convergence of nonlinear iteration for W, and consequently for C, provided that an accurate and efficient method is devised to carry out the inverse *Kirchhoff* transformation of (3.1).

It is nontrivial to compute this inverse *Kirchhoff* transformation directly [41,40]. One relatively simple but costly approach is Look-Up Table (LUT) method, namely, searching a corresponding value of C in a sorted data table between W and C by bisection. To this end, we need to set up a relational data table first by discretizing interval $[0, C_{\max}]$ and computing W at each discrete point of C in this interval in terms of *Kirchhoff* transformation (3.1), where $C_{\max}$ is the predictable upper-bound concentration due to the facts $0 \leqslant s \leqslant 1$ and (2.8). Then by bisection search and linear interpolation, we can quickly find out the corresponding value of C in this data table at any certain value of W. The finer the table is, the more accurate the solution C but more computational costs on bisectional search.

The left figure of Fig. 3.1 shows that W change very little when $C \to C_{\text{sat}}^{+} = 16^{+}$, implying that a small change in W in this region results in a large difference in C. Therefore we have to sufficiently refine the relational table especially around C_{sat} in order to accurately obtain the concentration C from W. Large computational cost results from the frequent search of such extra fine relational data to update C for each single value of W. Therefore, designing a robust and efficient method to evaluate C from W is necessary.

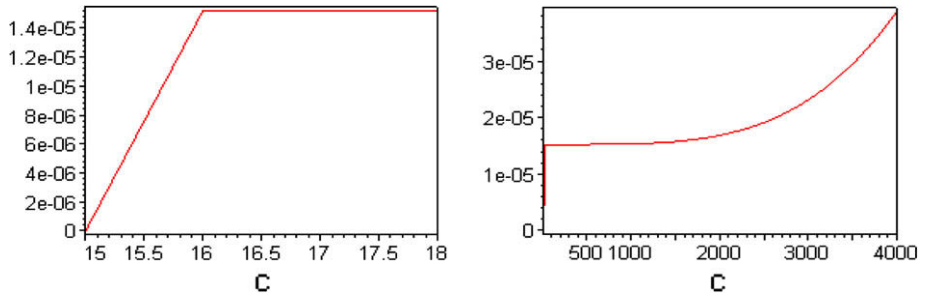

Fig. 3.1. $W(C)$ *(left)*in the region of $C \to C_{sat} = 16$; *(right)*in two-phases region ($C \geqslant C_{sat} = 16$).

Considering $W(C)$ is a strictly increasing continuous function with respect to C, in the following we develop a method which is much more efficient than the LUT method for evaluation of both *Kirchhoff* transformation and its inverse. We first notice the trivial case that if $C \leqslant C_{sat}$ or $W \leqslant W_s \equiv \int_0^{C_{sat}} \Gamma(\omega)d\omega$, then W is just a simple linear function of C by (3.2).

The nontrivial case is when $C > C_{sat}$ or $W > W_s$, in this case

$$W(C) = W_s + W_d(C) \tag{3.8}$$

where $W_d(C) = \int_{C_{sat}}^{C} \Gamma_{capdiff}(\omega)\, d\omega$.

The first simple observation is that we can explicitly evaluate $W_d(C)$ as an elementary function of C by determining the definite integration of $\Gamma_{capdiff}(\omega)$ with any symbolic operation software such as *Mathematica*, *Matlab* or *Maple*. This is feasible since capillary diffusion coefficient $\Gamma_{capdiff}(C)$ is well defined in (2.7) with respect to concentration C only. In consequence, the inverse *Kirchhoff* transformation can be evaluated by applying *Newton*'s method to (3.8) for any given $W > W_s$. Observing that the derivative of $W_d(C)$ is just $\Gamma_{capdiff}(C)$, we have the following *Newton*'s scheme for inverse *Kirchhoff* transformation:

$$C^{k+1} = C^k - \frac{W_s - W + W_d(C^k)}{\Gamma_{capdiff}(C^k)}, \quad k = 0, 1, 2, \ldots \tag{3.9}$$

where each term is given or computable. This scheme converges provably in very few steps with a proper initial guess C^0, according to the local quadratic convergence theory of *Newton*'s method. *Newton*'s approach (3.10) indeed provides an efficient way to evaluate C from W when $C > C_{sat}$, even when $C \to C_{sat}^{+}$. For the case of $C \leqslant C_{sat}$, linear function (3.3) is sufficient to get desired concentration.

In practice, the denominator $\Gamma_{capdiff}(C^k)$ in (3.9) approaches zero if C^k approaches C_{sat} in the two-phase region. In order to avoid this, a relative small positive number ε may be added to $\Gamma_{capdiff}(C^k)$ as follows:

$$C^{k+1} = C^k - \frac{W_s - W + W_{d,\varepsilon}(C^k)}{\Gamma_{capdiff}(C^k) + \varepsilon}, \quad k = 0, 1, 2, \ldots \tag{3.10}$$

where $W_{d,\varepsilon}(C) = \int_{C_{sat}}^{C} (\Gamma_{capdiff} + \varepsilon)(\omega)\, d\omega = \int_{C_{sat}}^{C} \Gamma_{capdiff}(\omega)d\omega + \varepsilon(C - C_{sat})$.

In comparison with Look-Up Table method, the computational cost of *Newton*'s approach is much smaller due to its fast convergence, with an approximate solution obtained under the tolerance of relative error 10^{-10} within averagely 12 iterations. In Section 6 we will implement inverse *Kirchhoff* transformation in terms of *Newton*'s method in fully implicit finite element-upwind finite volume discretization for (2.1) and (2.5).

Notice that the interfacial conditions at the GDL/channel interface (3.7c) and (3.7d) or (3.6) are always true no matter the gas channel is dry or wet, therefore (3.7) holds for both cases of dry and wet channels.

4. Nonlinear *Dirichlet–Neumann* alternating iteration

In the case of a wet gas channel, owing to the discontinuity of diffusivity at the GDL/channel interface, a new discontinuity is introduced for *Kirchhoff*'s variable W at the interface in reformulated water concentration Eq. (3.7), i.e. $W_1 \neq W_2$on part of Σ where $C \geqslant C_{sat}$.

In order to overcome the discontinuity of W at the GDL/channel interface for a wet channel, and at the same time maintain C and the mass flux continuous across Σ, as shown in (3.7), we consider the *Dirichlet–Neumann* alternating iteration algorithm [6] applied to the reformulated water concentration Eq. (3.7).

First of all, for the simplicity of notations, let us redefine *Kirchhoff* transformation as follows:

$$W_i(x) := \kappa_i(C_i(x)) = \int_0^{C_i(x)} \Gamma_i(c)dc \quad \text{in}\Omega_i, \quad i = 1, 2, \tag{4.1}$$

where $\kappa_i (i = 1,2)$ represent the restriction of *Kirchhoff* transformation in Ω_1 (GDL) and Ω_2 (gas channel), respectively. Moreover, $\Gamma_1 = \Gamma(C)$ and $\Gamma_2 = D_g^{eff}$, as defined in (2.5). Hence,

$$C_i = \kappa_i^{-1}(W_i), \quad i = 1,2, \tag{4.2}$$

where κ_1^{-1} is implemented by (3.10), and κ_2^{-1} is defined by (3.3).

In the case of a wet channel, if $C \geqslant C_{sat}$ somewhere on Σ, then $\Gamma_1 = \Gamma_{capdiff}$ by (2.6). However, since $\Gamma_2 = D_g^{eff} \neq \Gamma_1$, $W_1 \neq W_2$ is then introduced in that place on Σ. This does not happen to the case of a dry channel in which $C < C_{sat}$ everywhere on Σ and thus $\Gamma_1 = \Gamma_2$.

Considering the continuity of C on Σ:

$$C_1|_\Sigma = C_2|_\Sigma \quad \text{or} \quad \kappa_1^{-1}(W_1|_\Sigma) = \kappa_2^{-1}(W_2|_\Sigma) \tag{4.3}$$

and the equal mass flux of (3.7) across Σ:

$$(\nabla W_1 - \gamma_c C_1 \vec{u}) \cdot \overrightarrow{n_1} = -(\nabla W_2 - \vec{u} C_2) \cdot \overrightarrow{n_2} = -(\nabla W_2 - (D_g^{eff})^{-1} \vec{u} W_2) \cdot \overrightarrow{n_2}, \tag{4.4}$$

Thus we are able to split (3.7) into two subproblems as follows.

Q1: Dirichlet-type interfacial boundary value subproblem: By means of *Kirchhoff* transformation $\kappa_i (i = 1,2)$, we define the following well-posed P.D.E. in subdomain Ω_1 (GDL), which is equipped with *Dirichlet* boundary condition on interface Σ. Given $\vec{u} \in [H^2(\Omega)]^2$ and $W_2 \in H^2(\Omega_2)$, find $W_1 \in H^2(\Omega_1)$, such that

$$(Q1)\begin{cases} \Delta W_1 = \nabla \cdot (\gamma_c \vec{u} \kappa_1^{-1}(W_1)) \quad \text{in } \Omega_1 & (a) \\ W_1 = \kappa_1(\kappa_2^{-1}(W_2)) \quad \text{on } \Sigma & (b) \\ \frac{\partial W_1}{\partial n} - \gamma_c \vec{u} \kappa_1^{-1}(W_1) \cdot \vec{n} = \frac{I}{2F} \quad \text{on } (\partial\Omega)_6 & (c) \\ \frac{\partial W_1}{\partial n} = 0 (\partial\Omega)_2, (\partial\Omega)_4 & (d) \end{cases} \tag{4.5}$$

where (4.3) is applied to get (4.5b), W_2 will be iteratively updated in (4.5b) by solving the following subproblem *Q2*.

Q2: Neumann-type interfacial boundary value subproblem: In subdomain Ω_2 (gas channel), we define the following well-posed P.D.E. with *Robin*-like boundary condition on Σ. Given $\vec{u} \in [H^2(\Omega)]^2$ and $W_1 \in H^2(\Omega_1)$, find $W_2 \in H^2(\Omega_2)$, such that

$$(Q2)\begin{cases} -\Delta W_2 + \nabla \cdot ((D_g^{eff})^{-1} \vec{u} W_2) = 0 \quad \text{in } \Omega_2 & (a) \\ (\nabla W_2 - (D_g^{eff})^{-1} \vec{u} W_2) \cdot \overrightarrow{n_2} = -(\nabla W_1 - \gamma_c \kappa_1^{-1}(W_1) \vec{u}) \cdot \overrightarrow{n_1} \quad \text{on } \Sigma & (b) \\ W_2 = W_{\text{in}} \quad \text{on } (\partial\Omega)_1 & (c) \\ \frac{\partial W_2}{\partial n} = 0 (\partial\Omega)_3, (\partial\Omega)_5 & (d) \end{cases} \tag{4.6}$$

where (4.6b) is posted by the fact (4.4), W_1 will be iteratively updated in (4.6b) by solving subproblem *Q1*. Both subproblems *Q1* and *Q2* own *Dirichlet* boundary conditions, which ensure their well-posedness.

The definitions of subproblems *Q1* and *Q2* imply that we need to solve subproblems *Q1* and *Q2* iteratively for $(W_1, W_2) \in H^2(\Omega_1) \times H^2(\Omega_2)$ with an appropriate initial guess (W_1^0, W_2^0). Such iteration is usually called *Dirichlet–Neumann* alternating iteration method.

In order to formulate the *Dirichlet–Neumann* algorithm in a weak formulation, we introduce the following spaces $V_1 := H^1(\Omega_1), V_2 := \{v_2 \in H^1(\Omega_2) | v_2|_{(\partial\Omega)_1} = 0\}, \bar{V}_2 := \{v_2 \in H^1(\Omega_2) | v_2|_{(\partial\Omega)_1} = W_{\text{in}}\}, V_1^0 := \{v_1 \in V_1 | v_1|_\Sigma = 0\}, V_2^0 := \{v_2 \in V_2 | v_2|_\Sigma = 0\}, \Lambda := \{\lambda \in H^{\frac{1}{2}}(\Sigma) | \lambda = v|_\Sigma, v \in V_2\}$. The space Λ is equipped with a norm $\|\lambda\|_\Lambda := \inf_{v|_\Sigma = \lambda, v \in V_2} \|v\|_{1,\Omega_2}$. Since the diffusivity Γ_2 is constant, by the definition of *Kirchhoff* transformation (4.1), κ_2^{-1}: $\Lambda \to \Lambda$ is an isomorphism. The operator κ_1 is strictly monotonically increasing and Lipschitz continuous, thus $\|\kappa_1 \lambda\|_{\frac{1}{2},\Sigma} \leqslant \|\kappa_1\|_{\infty,\Sigma} \|\lambda\|_{\frac{1}{2},\Sigma} \leqslant C\|\lambda\|_\Lambda$, where the norm of $H^{\frac{1}{2}}(\Sigma)$ is defined as

$$\|\lambda\|_{\frac{1}{2},\Sigma}^2 = \|\lambda\|_{0,\Sigma}^2 + \int_\Sigma \int_\Sigma \frac{|\lambda(x) - \lambda(y)|^2}{|x - y|^2} \, dx \, dy.$$

This implies $\kappa_1 \kappa_2^{-1}$ maps Λ to $H^{\frac{1}{2}}(\Sigma)$, which is required in (4.7b).

By using $(\cdot,\cdot)_\Omega$ and $(\cdot,\cdot)_{\Omega_i}$ to stand for the L^2 inner product in Ω and $\Omega_i (i = 1,2)$, respectively, we define nonlinear *Dirichlet–Neumann* alternating iteration scheme for (3.7) in terms of the weak form as follows. Given $\lambda_2^0 \in \Lambda$, first of all, find $W_1^{k+1} \in V_1$ for each $k \geqslant 0$ such that

$$\begin{cases} (\nabla W_1^{k+1}, \nabla v_1)_{\Omega_1} = (\gamma_c \vec{u} \kappa_1^{-1}(W_1^k), \nabla v_1)_{\Omega_1} + \int_{(\partial\Omega)_6} \frac{I(\omega)}{2F} v_1 \, d\omega, \quad \forall \ v_1 \in V_1^0 & (a) \\ W_1^{k+1}|_\Sigma = \kappa_1\left(\kappa_2^{-1}(\lambda_2^k)\right), \quad \text{on } \Sigma & (b) \end{cases} \tag{4.7}$$

Let R_i (i=1, 2) be any continuous extension operator from Λ to V_i. Then in terms of the latest $W_1^{k+1} \in V_1$ obtained from (4.7), we successively find $W_2^{k+1} \in \bar{V}_2$ for each $k \geqslant 0$ such that

$$\begin{cases} (\nabla W_2^{k+1}, \nabla v_2)_{\Omega_2} - ((D_g^{eff})^{-1} \vec{u} W_2^{k+1}, \nabla v_2)_{\Omega_2} = -\int_{(\partial\Omega)_3} (D_g^{eff})^{-1} \vec{u} W_2^{k+1} \cdot \vec{n} v_2 \, d\omega, \quad \forall \ v_2 \in V_2^0 & (a) \\ (\nabla W_2^{k+1}, \nabla R_2 \mu)_{\Omega_2} - ((D_g^{eff})^{-1} \vec{u} W_2^{k+1}, \nabla R_2 \mu)_{\Omega_2} + \int_{(\partial\Omega)_3} (D_g^{eff})^{-1} \vec{u} W_2^{k+1} \cdot \vec{n} R_2 \mu \, d\omega & \\ \quad = -(\nabla W_1^{k+1}, \nabla R_1 \mu)_{\Omega_1} + (\gamma_c \vec{u} \kappa_1^{-1}(W_1^k), \nabla R_1 \mu)_{\Omega_1} + \int_{(\partial\Omega)_6} \frac{I(\omega)}{2F} R_1 \mu \, d\omega, \quad \forall \mu \in \Lambda & (b) \end{cases} \tag{4.8}$$

and set

$$\lambda_2^{k+1} = \theta W_2^{k+1}|_\Sigma + (1-\theta)\lambda_2^k, \tag{4.9}$$

where $\lambda_2^{k+1} \in \Lambda,\ \theta \in (0,1)$ is damping parameter.

In particular, for given $\mu \in \Lambda$, we choose harmonic extension $R_1\mu$ with Dirichlet boundary data μ on Σ, and homogeneous Neumann boundary conditions on other boundaries of Ω_1; also choose harmonic extension $R_2\mu$ with Dirichlet boundary data μ on Σ, zero on $(\partial\Omega)_1$, and homogeneous Neumann boundary conditions on other boundaries of Ω_2.

Obviously, (4.7) corresponds to subproblem *Q1*, and (4.8) is associated with subproblem *Q2*.

The algorithm of implementing nonlinear *Dirichlet–Neumann* alternating iteration scheme (4.7)–(4.9) is given in the following:

Algorithm A1. For $k \geqslant 0$,

1. Solve (4.7) for W_1^{k+1} with λ_2^k first.
2. Solve (4.8) for W_2^{k+1} with W_1^{k+1} secondly.
3. Update λ_2^{k+1} with W_2^{k+1} and λ_2^k in terms of (4.9), and determine if the following stopping criteria hold:

$$\|\lambda_2^{k+1} - \lambda_2^k\|_{L^2(\Sigma)} < \text{tolerance}.$$

If yes, stop. Otherwise, go back to the first step and continue.

The convergence of above *Dirichlet–Neumann* alternating iteration method for a nonlinear diffusion equation (without convection term) in one dimension can be theoretically proved in [6]. For our general convection–diffusion equation it is still an open question. However, numerical results shown in Section 7 suggest that this method converges uniformly with respect to the mesh size h.

As mentioned in Section 3, this method can be applied to the case of a dry channel as well. In Section 7, we will numerically verify the validity of our method presented in this section for both dry and wet channels.

5. Combined finite element-upwind finite volume methods

In comparison to the relatively small diffusion coefficients, the convection coefficients arising in momentum and concentration equations are dominant due to large flow present in the gas channel, which inevitably induces numerical instability and solution oscillations. It is crucial to design a robust numerical scheme to efficiently solve convection-dominated diffusion equations. This is another difficulty that prevents the entire nonlinear iteration from convergence besides the discontinuous and degenerate diffusivity in the water concentration equation. In this section we study an efficient scheme, which appropriately fits in the framework of finite element method, to automatically deal with the dominant convection terms arising from momentum and water concentration equations.

To deal with the dominant convection terms, in principle, upwind scheme is usually adopted for finite-difference method and finite-difference based finite volume method [21,19,20], versus the methods of artificial viscosity in the framework of finite element method such as streamline-diffusion scheme [17,16,23,28,34] and *Galerkin*-least-squares scheme [14,38,39,10] for convection-dominated diffusion problems and *Navier–Stokes* equations with high *Reynolds* number.

Due to the advantages of utilizing finite element method to conveniently deal with an irregular domain, flux (*Neumann*) boundary conditions, and most importantly, provide a highly accurate approximation to the real solution, we primarily choose finite element method to discretize a well-posed partial differential equation with given boundary conditions. However, for convection-dominated problems, the methods of artificial viscosity are just barely satisfactory, because their stabilization parameters, on the magnitude of $O(h)$, are difficult to properly choose for nonlinear problems. Therefore, the upwind scheme turns out to be a better choice in a manner of automatically updating its upwind parameter although it cannot directly work for finite element method due to its finite-difference based feature.

In order to combine all the power of both finite element method and upwind scheme together, we introduce a combined finite element-upwind finite volume method [12,13,11] for the PEFC model in this section, where a finite volume based finite-difference upwind scheme is adopted to specifically deal with dominant convection term only, meanwhile, all the other terms are still discretized by finite element method. By doing this, we are able to take into account the irregular domain and natural boundary condition as well as dominant convection term without tuning any stabilization parameters.

Without loss of generality, let us choose (4.8a) as an example to demonstrate how the combined finite element-upwind finite method works for the PEFC model. In the following we will employ finite element method to discretize the diffusion (*Laplacian*) term, and describe how to apply upwind finite volume method to the convection term in (4.8a).

To discretize weak form (4.8a) with finite element method for a certain iteration step k (for simplicity, we omit k in this section), we firstly choose finite element space $V_h^2 \subset \bar{V}_2$ which consists of piecewise linear polynomial on a quasi-uniform mesh $\mathcal{T}_{2,h}$ with mesh size h in $\Omega_{2,h}$ (a polygonal approximation of the domain Ω_2). We define the following finite element discretization for (4.8a). Find $W_{h,2} \in V_h^2$ such that for any $v_h \in V_{h,0}^2 \subset V_2^0$

$$(\nabla W_{h,2}, \nabla v_h)_{\Omega_{2,h}} - \left((D_g^{eff})^{-1}\vec{u}W_{h,2}, \nabla v_h\right)_{\Omega_{2,h}} + \int_{(\partial\Omega)_3} (D_g^{eff})^{-1}\vec{u}W_{h,2}\cdot\vec{n}\, v_h\, d\omega = 0. \tag{5.1}$$

where $(\cdot,\cdot)_{\Omega_{2,h}}$ stands for the L^2 inner product in $\Omega_{2,h}$. The diffusion term in (5.1) is suited for finite element discretization. Here we introduce an upwind finite volume scheme to deal with the convection term in (5.1).

First, we reformulate (5.1) into a new discretization form containing the true divergent-type convection term as follows:

$$\left(\nabla W_{h,2}, \nabla v_h\right)_{\Omega_{2,h}} + \left(\nabla\cdot((D_g^{eff})^{-1}\overrightarrow{u}W_{h,2}), v_h\right)_{\Omega_{2,h}} - \int_{\Sigma}\left((D_g^{eff})^{-1}\overrightarrow{u}W_{h,2}\right)\cdot\overrightarrow{n_2}\, v_h\, d\omega = 0. \tag{5.2}$$

where, the boundary integral term on $(\partial\Omega)_3$ vanishes because it is remerged to the divergent-type convection term, and a new interfacial boundary integral term on Σ appears instead.

For the simplicity of notations, let us begin with a generic divergent-type convection term in weak form $(\nabla\cdot(\overrightarrow{\beta}p), q)$ first, where $\overrightarrow{\beta}$ is a known large vector, p and q are the trial and test functions, respectively, which all belong to the same finite element space V_h^2.

Let $\mathcal{P}_h = \{P_i; i\in J\}$ be the set of all vertices of all element $T\in\mathcal{T}_{2,h}$, where J is a suitable index set. We let $\hat{J} = \{i\in J; P^i\in\Omega^{2,h}\}$ to represent the set of interior vertices in $\Omega_{2,h}$, i.e. those vertices which locate on $\partial\Omega_{2,h}$ are not counted in $\hat{J}$. Now let us construct the dual mesh $\mathcal{D}_h = \{\Omega_i; i\in\hat{J}\}$ over the basic mesh $\mathcal{T}_{2,h}$. The dual finite volume Ω_i associated with a vertex $P_i\in\mathcal{P}_h$ is a closed polygon obtained in the following way: we join the center of gravity of every element $T\in\mathcal{T}_{2,h}$ that contains the vertex P_i with the center of every side of T containing P_i. If $P_i\in\mathcal{P}_h\cap\partial\Omega_{2,h}$, then we complete the obtained contour by the straight segments joining P_i with the centers of boundary sides (i.e. sides which are subsets of $\partial\Omega_{2,h}$) that contain P_i. In this way, we get the boundary $\partial\Omega_i$ of the finite volume Ω_i. (See Fig. 5.1). It is obvious that $\overline{\Omega_{2,h}} = \bigcup_{i\in\hat{J}}\Omega_i$. The interiors of $\Omega^i, i\in\hat{J}$, are mutually disjoint.

Based on above dual mesh $\mathcal{D}_h$, we derive the following finite volume discretization:

$$\begin{aligned}(\nabla\cdot(\overrightarrow{\beta}p), q)_{\Omega} &= \sum_{i=1}^{N}\int_{\Omega_i}\nabla\cdot(\overrightarrow{\beta}p)q\,dx \approx \sum_{i=1}^{N} q_i\int_{\Omega_i}\nabla\cdot(\overrightarrow{\beta}p)\,dx = \sum_{i=1}^{N} q_i\oint_{\partial\Omega_i}(\overrightarrow{\beta}\cdot\overrightarrow{n})p\,ds\\ &= \sum_{i=1}^{N} q_i\sum_{P_j\in\partial\Lambda_i}\int_{\Gamma_{ij}}(\overrightarrow{\beta}\cdot\overrightarrow{n})p\,ds \approx \sum_{i=1}^{N} q_i\sum_{P_j\in\partial\Lambda_i}\int_{\Gamma_{ij}}(\overrightarrow{\beta}\cdot\overrightarrow{n})p_{m_{ij}}\,ds\\ &\approx \sum_{i=1}^{N} q_i\sum_{P_j\in\partial\Lambda_i}\int_{\Gamma_{ij}}(\overrightarrow{\beta}\cdot\overrightarrow{n})(r_{ij}p_i + (1-r_{ij})p_j)\,ds,\end{aligned} \tag{5.3}$$

where Ω_i is the control volume of vertex P_i, which is encompassed by its patch Λ_i, Fig. 5.1 shows a patch Λ_1 associated with vertex P_1, and $P_j\in\partial\Lambda_1 (j\neq 1)$. Γ_{ij} is a portion of $\partial\Omega_i$, the internal lines which intersect with element edge $e_{ij} = \overline{P_iP_j}$ at midpoint m_{ij}, therefore $\partial\Omega_i = \sum_{P_j\in\partial\Lambda_i}\Gamma_{ij}$.

In (5.3) we make three approximations. The first is the approximation of test function q in the control volume Ω_i with the evaluation of q at vertex P_i. The second approximation is made for the numerical quadrature of trial function p in the boundary integration on Γ_{ij}, where we use $p_{m_{ij}}$ by evaluating p at the midpoint m_{ij} of the intersected edge e_{ij}. In the third approximation, we introduce upwind scheme to calculate $p_{m_{ij}}$:

$$p_{m_{ij}} = r_{ij}p_i + (1-r_{ij})p_j, \tag{5.4}$$

where r_{ij} is the upwind parameter, automatically determined by the following formula:

$$r_{ij} = \begin{cases} 1 & \text{if } F_{ij} > 0,\\ 0 & \text{if } F_{ij} < 0,\\ 0.5 & \text{if } F_{ij} = 0,\end{cases} \tag{5.5}$$

where $F_{ij} = \int_{\Gamma_{ij}}(\overrightarrow{\beta}\cdot\overrightarrow{n})\,ds$ is called numerical flux. (5.5) implies $r_{ij} + r_{ji} = 1$. By numerical flux F_{ij}, (5.3) can be rewritten as

$$(\nabla\cdot(\overrightarrow{\beta}p), q)_{\Omega} \approx \sum_{i=1}^{N} q_i\sum_{P_j\in\partial\Lambda_i} F_{ij}(r_{ij}p_i + (1-r_{ij})p_j) = \sum_{i=1}^{N} q_i\sum_{P_j\in\partial\Lambda_i}\int_{\Gamma_{ij}}(\overrightarrow{\beta}\cdot\overrightarrow{n})\,ds(r_{ij}p_i + (1-r_{ij})p_j). \tag{5.6}$$

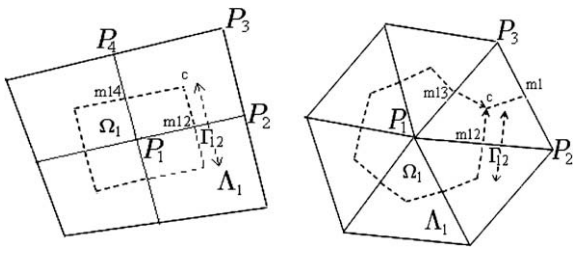

Fig. 5.1. Control volume Ω_1 in 2D dual mesh encompassed by broken lines in patch Λ_1.

Apparently $F_{ij} = -F_{ji}$.

In (5.6) it is crucial to correctly compute numerical flux F_{ij} in 2D rectangle or triangle elements, as shown in Fig. 5.1. To this end, we need to calculate the dot product of average convective vector $\vec{\beta}_{av}$ and outer normal vector $\vec{n}$ on each line segment contained in Γ_{ij}, then the sum of the numerical fluxes at each line segment gives birth to F_{ij}, where one of the endpoint of each line segment locates at the midpoint m_{ij} of line segment $\overline{P_iP_j}$, and the other endpoint is the element center c.

Average convective vector $\vec{\beta}_{av}$ can be easily obtained by averaging $\vec{\beta}$ at two endpoints of each line segment. We define dot product $\vec{\beta}_{av} \cdot \vec{n}$ on each line segment of Γ_{ij} in terms of the unit orthogonal vector $\vec{t}$ of $\vec{n}$. For instance, on the line segment $\overline{m_{ij}c}$ in Fig. 5.1, we take $\vec{t} = \frac{\overrightarrow{m_{ij}c}}{|\overrightarrow{m_{ij}c}|}$. Then $\vec{n} \cdot \vec{t} = 0$. The following identity holds for two orthogonal vectors $\vec{n}$ and $\vec{t}$ in two-dimensional space:

$$|\vec{\beta}_{av} \cdot \vec{n}| = |\vec{\beta}_{av} \times \vec{t}|, \tag{5.7}$$

where, the sign of $\vec{\beta}_{av} \cdot \vec{n}$ is determined by the direction of cross product $\vec{\beta}_{av} \times \vec{t}$. By Right Hand Rule, if $\vec{\beta}_{av} \times \vec{t}$ points upward, then $\vec{\beta}_{av} \cdot \vec{n}$ is positive, otherwise negative. Thus, in practice, a partial numerical flux $F_{ij}|_{\overline{m_{ij}c}}$, which is the restriction of F_{ij} on the line segment $\overline{m_{ij}c}$, is approximated by Trapezoidal Rule of numerical quadrature as follows:

$$F_{ij}|_{\overline{m_{ij}c}} = \int_{\overline{m_{ij}c}} (\vec{\beta} \cdot \vec{n})\, ds \approx |\overrightarrow{m_{ij}c}|(\vec{\beta}_{av} \cdot \vec{n}).$$

Considering (5.7) and the definition of vector $\vec{t}$, we derive the magnitude of $F_{ij}|_{\overline{m_{ij}c}}$ as follows:

$$|F_{ij}|_{\overline{m_{ij}c}}| \approx |\overrightarrow{m_{ij}c}||\vec{\beta}_{av} \cdot \vec{n}| = |\vec{\beta}_{av} \times \overrightarrow{m_{ij}c}|.$$

Here the sign of $|F_{ij}|_{\overline{m_{ij}c}}|$ is determined by the direction of cross product $\vec{\beta}_{av} \times \overrightarrow{m_{ij}c}$ described as above.

By applying (5.6) to the divergent-type convection term in (5.2), we obtain the combined finite element-upwind finite volume discretization for (4.8a) as follows: find $W_{h,2} \in V_h^2$ such that for any $v_h \in V_{h,0}^2$

$$(\nabla W_{h,2}, \nabla v_h)_{\Omega_{2,h}} - \int_{\Sigma} \left((D_g^{eff})^{-1} \vec{u} W_{h,2} \right) \cdot \vec{n_2}\, v_h\, d\omega + \sum_{i=1}^{N} v_{h,i} \sum_{P_j \in \partial \Lambda_i} \int_{\Gamma_{ij}} \left[(D_g^{eff})^{-1} \vec{u} \cdot \vec{n} \right] ds \left(r_{ij} W_{h,2,i} + (1 - r_{ij}) W_{h,2,j} \right) = 0, \tag{5.8}$$

where upwind parameter r_{ij} is determined by (5.5), the corresponding numerical flux F_{ij} is defined as

$$F_{ij} = \int_{\Gamma_{ij}} \left[(D_g^{eff})^{-1} \vec{u}_h \cdot \vec{n} \right] ds.$$

We will also apply the same upwind finite volume scheme to the convection term in momentum Eq. (2.1a) in Section 6.

6. Numerical methods

In this section we design a decoupled finite element-upwind finite volume discretization for *Navier–Stokes* Eq. (2.1) with *Picard*'s linearization scheme and a reformulated water concentration Eq. (3.7) with nonlinear *Dirichlet–Neumann* alternating iteration scheme (4.7)–(4.9).

Picard's *linearization for Navier–Stokes Eq. (2.1)* With given $(\vec{u}^k, C^k)$ from the kth step, find $(\vec{u}^{k+1}, P^{k+1})$ such that for $k = 0, 1, 2, \ldots$

$$\begin{cases} \frac{1}{\varepsilon^2} \nabla \cdot (\rho^k \vec{u}^k \vec{u}^{k+1}) = \nabla \cdot (\mu^k \nabla \vec{u}^{k+1}) - \nabla P^{k+1} - \frac{\mu^k}{K} \vec{u}^{k+1}, \\ \nabla \cdot \vec{u}^{k+1} = -\frac{\nabla \rho^k}{\rho^k} \cdot \vec{u}^k, \end{cases} \tag{6.1}$$

where we reformulate (2.1b) to be $\nabla \cdot \vec{u} = -\frac{\nabla \rho}{\rho} \cdot \vec{u}$ in order to be consistent with pressure term in momentum equation (2.1a). Thus, an exact saddle-point problem is produced and the weak solutions of (6.1) are guaranteed by *Babuska–Brezzi–Ladyzhenskaya* condition [26].

Weak forms: we define the spaces $\Phi := \{\vec{v} = (v_x, v_y)^\top \in [H^1(\Omega)]^2 | v_x|_{(\partial\Omega)_1} = u_x|_{\text{inlet}}\}$ and $\Psi := L^2(\Omega)$. Then the mixed weak forms for (2.1) on the basis of *Picard*'s linearization (6.1) are presented as follows: find $(\vec{u}^{k+1}, P^{k+1}) \in \Phi \times \Psi$, such that for any $(\vec{v}, q) \in \Phi \times \Psi$

$$\begin{cases} (\mu^k \nabla \vec{u}^{k+1}, \nabla \vec{v})_\Omega + \left(\frac{1}{\varepsilon^2} \nabla \cdot (\rho^k \vec{u}^k \vec{u}^{k+1}), \vec{v} \right)_\Omega - (P^{k+1}, \nabla \cdot \vec{v})_\Omega + (\frac{\mu^k}{K} \vec{u}^{k+1}, \vec{v})_\Omega = 0 \\ (\nabla \cdot \vec{u}^{k+1}, q)_\Omega = -(\frac{\nabla \rho^k}{\rho^k} \cdot \vec{u}^k, q)_\Omega \end{cases} \tag{6.2}$$

In *Dirichlet–Neumann* alternating iteration scheme (4.7)–(4.9), *Picard*'s linearization method has been applied to the weak forms of *Q1* and *Q2*, the two subproblems of reformulated water concentration Eq. (3.7).

Combined finite element-upwind finite volume discretizations Corresponding to weak form (6.2), we apply mixed finite element method to *Navier–Stokes* Eq. (2.1), and standard finite element method to *Dirichlet–Neumann* alternating iteration scheme (4.7)–(4.9), except their convection terms which are discretized by upwind scheme.

First of all, along the GDL/gas channel interface Σ in Ω as shown in Fig. 2.2, we define a quasi-uniform triangulation $\mathcal{T}_h$ with the maximum mesh size h in Ω_h (a polygonal approximation of the domain Ω). Then $\mathcal{T}_h = \mathcal{T}_{1,h} \cup \mathcal{T}_{2,h}$, where $\mathcal{T}_{1,h}$ and $\mathcal{T}^{2,h}$ are a quasi-uniform mesh in $\Omega_{1,h}$ and $\Omega_{2,h}$, respectively. Obviously $\Omega_h = \Omega_{1,h} \cup \Omega_{2,h}$. Let $(\cdot,\cdot)_{\Omega_h}$ and $(\cdot,\cdot)_{\Omega_{i,h}}$ $(i = 1,2)$ stand for the L^2 inner product in Ω_h and $\Omega_{i,h}(i = 1,2)$, respectively.

To discretize weak form (6.2) in mixed finite element method, we introduce finite element space $S_h = \Phi_h \times \Psi_h \subset \Phi \times \Psi$ on $\mathcal{T}_h$, where Φ_h consists of piecewise quadratic functions, and Ψ_h consist of piecewise linear functions. S_h is exactly the well known space of *Taylor–Hood* element, one type of stable mixed finite element specifically for saddle-point variational problem [3]. The purpose of this choice for finite element space S_h is to approximate the velocity with quadratic element (P_2), and pressure and concentration with linear element (P_1), simultaneously, on the theoretical basis of *Babuska–Brezzi–Ladyzhenskaya* condition and its discrete form [26].

On the other hand, we employ the combined finite element-upwind finite volume method to discretize *Dirichlet–Neumann* alternating iteration scheme (4.7)–(4.9). We define finite element spaces as the following piecewise linear polynomial spaces $V_h^1 \subset V_1, V_{h,0}^1 \subset V_1^0$ on $\mathcal{T}_{1,h}$ and $V_h^2 \subset \bar{V}_2, V_{h,0}^2 \subset V_2^0$ on $\mathcal{T}_{2,h}$, and let $V_h = V_h^1 \oplus V_h^2$. Consequently, on the GDL/channel interface Σ, we define $\Lambda_h \in \Lambda$ as the space of piecewise linear finite elements in 1D, corresponding to the triangulation.

Let $R_{i,h}$ $(i = 1,2)$ be any continuous extension operator from Λ_h to V_h^i, and based on the weak forms (6.2), (4.7)–(4.9), we define the following decoupled mixed and standard finite element discretizations, combining with upwind finite volume scheme to deal with the dominant convection terms in momentum equation and concentration equation, respectively.

Find $(\vec{u}_h^{k+1}, P_h^{k+1}) \in S_h$ $(k = 0,1,2,\ldots)$, such that for any given $(\vec{v}, q) \in S_h$

$$\begin{cases} (\mu(C_h^k)\nabla\vec{u}_h^{k+1}, \nabla\vec{v})_{\Omega_h} - (P_h^{k+1}, \nabla\cdot\vec{v})_{\Omega_h} + \left(\frac{\mu(C_h^k)}{K}\vec{u}_h^{k+1}, \vec{v}\right)_{\Omega_h} \\ \quad + \sum_{i=1}^{N} v_i \sum_{P_j\in\partial\Lambda_i} \frac{1}{\varepsilon^2}\int_{\Gamma_{ij}} \left(\rho(C_h^k)\vec{u}_h^k\cdot\vec{n}\right) ds\left(r_{ij}\vec{u}_{h,i}^{k+1} + (1-r_{ij})\vec{u}_{h,j}^{k+1}\right) = 0 \quad (a) \\ (\nabla\cdot\vec{u}_h^{k+1}, q)_{\Omega_h} = -\left(\frac{\nabla\rho(C_h^k)}{\rho(C_h^k)}\cdot\vec{u}_h^k, q\right)_{\Omega_h}, \quad (b) \end{cases} \tag{6.3}$$

where r_{ij} is determined by (5.5) with the following numerical flux:

$$F_{ij} = \frac{1}{\varepsilon^2}\int_{\Gamma_{ij}} \left(\rho(C_h^k)\vec{u}_h^k\cdot\vec{n}\right) ds.$$

In (6.3), C_h^k is obtained from W_h^k in the iteration process by using inverse *Kirchhoff* transformation (3.10). Since $W_h^k \in V_h$, then $C_h^k \in V_h$ in view of the definition of *Kirchhoff* transformation and the fact that $\Gamma(C)$ is a rational function of C.

After $\vec{u}_h^{k+1}$ is obtained from (6.3), with a view to (5.8), we define the combined finite element-upwind finite volume discretizations for *Dirichlet–Neumann* alternating iteration scheme (4.7)–(4.9) as follows. Given $\lambda_{h,2}^0 \in \Lambda_h$, find $W_h^{k+1} = (W_{h,1}^{k+1}, W_{h,2}^{k+1}) \in V_h^1 \times V_h^2$, for each $k \geqslant 0$ such that

$$\begin{cases} \left(\nabla W_{h,1}^{k+1}, \nabla v_h^1\right)_{\Omega_{1,h}} = \left(\gamma_c\vec{u}_h^{k+1}\kappa_1^{-1}(W_{h,1}^k), \nabla v_h^1\right)_{\Omega_{1,h}} + \int_{(\partial\Omega)_6}\frac{I(\omega)}{2F}v_h^1 d\omega, \ \forall v_h^1 \in V_{h,0}^1 \quad (a) \\ W_{h,1|\Sigma}^{k+1} = I_h\kappa_1\left(\kappa_2^{-1}(\lambda_{h,2}^k)\right), \ \text{in}\Lambda \quad (b) \end{cases} \tag{6.4}$$

and

$$\begin{cases} \left(\nabla W_{h,2}^{k+1}, \nabla v_h^2\right)_{\Omega_{2,h}} - \int_\Sigma \left((D_g^{eff})^{-1}\vec{u}_h^{k+1}W_{h,2}^{k+1}\right)\cdot\overrightarrow{n_2}\, v_h^2 d\omega \\ \quad + \sum_{i=1}^{N_2} v_{h,i}^2 \sum_{P_j\in\partial\Lambda_i}\int_{\Gamma_{ij}}\left[(D_g^{eff})^{-1}\vec{u}_h^{k+1}\cdot\vec{n}\right] ds\left(r_{ij}W_{h,2,i}^{k+1} + (1-r_{ij})W_{h,2,j}^{k+1}\right) = 0, \quad \forall v_h^2 \in V_{h,0}^2 \quad (a) \\ (\nabla W_{h,2}^{k+1}, \nabla R_{2,h}\mu_h)_{\Omega_{2,h}} - \int_\Sigma \left((D_g^{eff})^{-1}\vec{u}_h^{k+1}W_{h,2}^{k+1}\right)\cdot\overrightarrow{n_2}\, R_{2,h}\mu_h d\omega \\ \quad + \sum_{i=1}^{N_2} R_{2,h}\mu_{h,i}\sum_{P_j\in\partial\Lambda_i}\int_{\Gamma_{ij}}\left[(D_g^{eff})^{-1}\vec{u}_h^{k+1}\cdot\vec{n}\right] ds\left(r_{ij}W_{h,2,i}^{k+1} + (1-r_{ij})W_{h,2,j}^{k+1}\right) \\ \quad = -(\nabla W_{h,1}^{k+1}, \nabla R_{1,h}\mu_h)_{\Omega_{1,h}} + (\gamma_c\vec{u}_h^{k+1}\kappa_1^{-1}(W_{h,1}^k), \nabla R_{1,h}\mu_h)_{\Omega_{1,h}} + \int_{(\partial\Omega)_6}\frac{I(\omega)}{2F}R_{1,h}\mu_h d\omega, \quad \forall\mu_h \in \Lambda_h \quad (b) \end{cases} \tag{6.5}$$

where I_h in (6.4b) represents a linear interpolation operator which maps any space of smooth functions into V_h^1. $R_{1,h}$ and $R_{2,h}$ are the discrete harmonic extensions of R_1 and R_2, respectively. N_2 denotes the number of grid points in triangulation $\mathcal{T}_2$. r_{ij} is determined by (5.5) with the following numerical flux

$$F_{ij} = \int_{\Gamma_{ij}}\left[(D_g^{eff})^{-1}\vec{u}_h^{k+1}\cdot\vec{n}\right] ds.$$

We update $\lambda_{h,2}^{k+1}$ with some damping parameter $\theta \in (0,1)$ as follows

$$\lambda_{h,2}^{k+1} := \theta W_{h,2|\Sigma}^{k+1} + (1-\theta)\lambda_{h,2}^{k}. \tag{6.6}$$

To numerically compute $\nabla W_{h,1}^{k+1}$ on the right hand side of (6.5), in practice, we employ the technique of global L^2 projection-recovered gradient [35]. In addition, $\nabla\rho(C)$ in both (6.3) and (6.5) can be rewritten as $\nabla\rho(C) = (\rho_l - \rho_g)\nabla s = (\rho_l - \rho_g)/(\frac{\rho_l}{M} - C_{\text{sat}})\nabla C$.

Numerical algorithms: we state the algorithm of implementing finite element discretizations (6.3)–(6.6) as follows.

Algorithm A2. For $k \geqslant 0$, given $\vec{u}_h^0, C_h^0$, the following procedures are successively executed:

1. Solve (6.3) for $(\vec{u}_h^{k+1}, P_h^{k+1})$ first.
2. In terms of Algorithm A1, solve (6.4)–(6.6) with given $\lambda_2^0 = \lambda_{h,2}^k$, and obtain $W_h^{k+1} = (W_{h,1}^{k+1}, W_{h,2}^{k+1})$ for $k \geqslant 0$.
3. Calculate C_h^{k+1} with W_h^{k+1} in terms of *Newton*'s method of inverse *Kirchhoff* transformation (3.10).
4. Determine if the following stopping criteria hold

$$\frac{\|\vec{u}_h^{k+1} - \vec{u}_h^k\|_{L^2(\Omega)} + \|P_h^{k+1} - P_h^k\|_{L^2(\Omega)} + \|\lambda_{h,2}^{k+1} - \lambda_{h,2}^k\|_{L^2(\Sigma)}}{\|\vec{u}_h^k\|_{L^2(\Omega)} + \|P_h^k\|_{L^2(\Omega)} + \|\lambda_{h,2}^k\|_{L^2(\Sigma)}} < \text{tolerance}, \tag{6.7}$$

which is the relative convergence error in two successive iteration steps. If yes, then numerical computation is complete. Otherwise, go back to the first step and continue.

Assignment of initial guesses: now we discuss the initial guesses $(\vec{u}_h^0, C_h^0)$ for (6.3)–(6.6). Although there is no certain way to specify the initial guesses, in practice, they can usually be given in terms of boundary conditions and physical phenomena. It is well known that the flow profile is parabolic once laminar flow is fully developed in long, straight channel, under steady-state conditions. Based on this fact, we are able to assign the initial profile of velocity as follows by preserving the same total flow flux with the case of constant horizontal velocity u_{in} at the inlet

$$\begin{aligned} (u_h^0)_x &= \begin{cases} \frac{\pi}{2} u_{\text{in}} \sin(\frac{y}{\delta_{\text{CH}}}\pi), x = 0, 0 \leqslant y \leqslant \delta_{\text{CH}} \ \text{(inlet)} \\ 0, \text{elsewhere} \end{cases} \\ (u_h^0)_y &= 0, W_h^0 = W_{\text{in}}, \end{aligned} \tag{6.8}$$

where $(u_h^0)_x$ is the x-component of $\vec{u}_h^0$. We use a sine function to approximate $(u_h^0)_x$ as a parabolic-like function at the inlet, an approximation of laminar flow in long, straight channel, whose the highest velocity u_{in} (m/s) occurs at the center of inlet ($y = \frac{\delta_{\text{CH}}}{2}$) and quadratically decays to zero on the boundary wall. This initial guess is close to the real case of parabolic flow in the gas channel, thus helping to attain good convergence for nonlinear iteration. As a consequence, in the following numerical experiments, we assign the *Dirichlet* boundary condition of velocity at the inlet as follows

$$u_x|_{\text{inlet}} = \frac{\pi}{2} u_{\text{in}} \sin(\frac{y}{\delta_{\text{CH}}}\pi), \quad 0 \leqslant y \leqslant \delta_{\text{CH}}. \tag{6.9}$$

Considering *Kirchhoff* transformation (3.1) does not depend on the spatial domain but only concentration variable, we can directly generalize it to the three-dimensional situation. Consequently numerical discretizations (6.3)–(6.6) are readily extendable to a three-dimensional PEFC model without any difficulty.

7. Numerical experiments

The inlet velocity of air and current density I at the membrane/cathode surface significantly affect the distribution of water in both gas channel and GDL. A smaller entry velocity ($u_{\text{in}} < 3$ m/s), which experiences rapid saturation of the gas phase by water vapor, results in a wet channel filled partially with liquid water. Similarly, higher transfer current density I creates a two-phase region in the gas channel.

In this section, we illustrate these physical expectations with the numerical methods mentioned in Section 6 by varying inlet velocities and current densities I for a wet channel in Case 1, 2 and a dry channel in Case 3, through which, we simultaneously exhibit the efficiency, accuracy of our new numerical techniques, and the generality of our *Dirichlet–Neumann* alternating iterative domain decomposition method for both dry and wet channels.

We firstly define triangulation $\mathcal{T}_h$ with *20* intervals in the length of fuel cell along x-direction, *30* and *25* intervals in the width of gas channel and GDL, respectively, along y-direction. So the number of total grid points in $\mathcal{T}_h$ is $(20+1)\times(30+25+1) = 1176$. The tolerance of our stopping criteria (6.7) for the outer nonlinear iteration in Algorithm A2 and inner nonlinear iteration in Algorithm A1 are all 10^{-10}. In the following numerical experiments, we adopt a single damping parameter of $\theta = 0.8$ for our *Dirichlet–Neumann* alternating iteration method in Algorithm A1. To solve the discretized linear algebraic system, we employ a direct solver and GMRES iterative solver, depending on the number of degree of freedom.

Case 1: C_{in} = 14 mol/m^3,u_{in} = 2 m/s, average current density I = 1.5 A cm^{-2}: we create a wet channel case by reinforcing C_{in} = 14 mol/m^3,u_{in} = 2 m/s at the inlet of gas channel, and assign liquid water mass flux condition at the membrane/cathode surface with average current density $I = \frac{I_1+I_2}{2} = 1.5$ A cm^{-2}. By employing numerical discretizations (6.3)–(6.6) and Algorithm A1 and Algorithm A2, we obtain a reasonable solution (see Figs. 7.3–7.8) within 11 outer nonlinear iteration steps in Algorithm A2, and up to 14 inner *Dirichlet–Neumann* alternating iteration steps in Algorithm A1. Fig. 7.1 displays the fast convergence process with *Kirchhoff* transformation and *Dirichlet–Neumann* alternating iteration method, and oscillating iteration without *Kirchhoff* transformation, respectively.

As an example, in this case we do more computations to display the uniform convergence of *Dirichlet–Neumann* alternating iterative domain decomposition method in Algorithm A1. Table 7.1 shows the iteration history of this method for Case 1, specifically. It is typically produced for the first outer nonlinear iteration step in Algorithm A2, where the velocity is given by initial guess (6.8). In Table 7.1, we find that the number of nonlinear iteration step is independent of the mesh size h, which is always *14* iterations along with decreasing h under the same tolerance of iteration stopping criteria 10^{-10}. Here the maximum mesh size $h = \frac{l_{PEFC}}{k}$, where k is the number of mesh interval in the length of PEFC and the width of gas channel, as well as $k/2$ in the width of GDL.

Fig. 7.2 displays a similar convergence path on each globally refined mesh level for *Dirichlet–Neumann* alternating iteration method, which is a quasi-linearly converging process with respect to iteration number, and independent of maximum mesh size h as well.

In the following, the focus is placed on elucidating numerical results shown in Figs. 7.3–7.8, where the interface of gas channel and GDL is indicated by a bold line.

Figs. 7.3–7.6 shows the velocity field of the two-phase mixture in the GDL and gas channel. As expected, there is a large difference in the velocity scale between the porous region and the open channel. The mixture velocity in GDL is at least two orders of magnitude smaller than that in the open channel, indicating that gas diffusion is the dominant transport mechanism in porous GDL. The flow field in the open channel is fully developed in view of the large aspect ratio of the channel, as can be seen in Fig. 7.6 where the channel length is, however, not drawn to scale for better view.

The figure at the bottom of Fig. 7.7 displays the water concentration distribution whose value is below C_{sat}, indicating absence of liquid water in the porous cathode and flow channel. As the air flows down the channel, water is continuously added by the electrochemical reaction, resulting in an increased water vapor concentration along the channel. As a result, liquid water may first appear in the vicinity of the membrane/cathode interface towards the channel outlet, and gradually

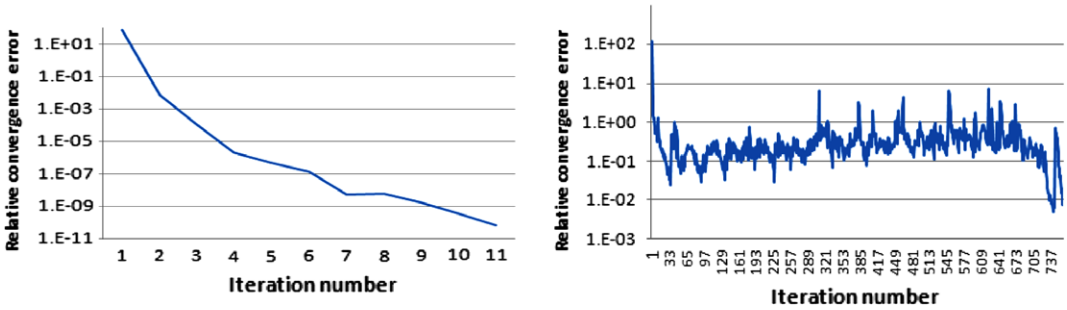

Fig. 7.1. Iteration histories of *(left)* FEM with Kirchhoff transformation and Dirichlet–Neumann alternating iteration; *(right)* standard FEM without Kirchhoff transformation and with Picard's iteration.

Table 7.1
Nonlinear iteration information of Dirichlet–Neumann alternating iteration with decreasing maximum mesh size $h = \frac{l_{PEFC}}{k}$.

Step	k = 8	k = 16	k = 32	k = 64	k = 128	k = 256
1	6.121E-02	7.447E-02	8.176E-02	8.558E-02	8.753E-02	8.852E-02
2	1.223E-02	1.487E-02	1.632E-02	1.708E-02	1.746E-02	1.766E-02
3	2.435E-03	2.956E-03	3.241E-03	3.390E-03	3.467E-03	3.506E-03
4	4.846E-04	5.871E-04	6.433E-04	6.727E-04	6.878E-04	6.955E-04
5	9.643E-05	1.166E-04	1.277E-04	1.335E-04	1.364E-04	1.380E-04
6	1.918E-05	2.316E-05	2.533E-05	2.648E-05	2.707E-05	2.737E-05
7	3.817E-06	4.598E-06	5.027E-06	5.253E-06	5.369E-06	5.429E-06
8	7.594E-07	9.132E-07	9.974E-07	1.042E-06	1.065E-06	1.077E-06
9	1.511E-07	1.814E-07	1.979E-07	2.068E-07	2.113E-07	2.136E-07
10	3.006E-08	3.602E-08	3.928E-08	4.102E-08	4.192E-08	4.238E-08
11	5.980E-09	7.153E-09	7.794E-09	8.138E-09	8.316E-09	8.406E-09
12	1.190E-09	1.421E-09	1.547E-09	1.615E-09	1.650E-09	1.668E-09
13	2.367E-10	2.821E-10	3.069E-10	3.203E-10	3.273E-10	3.308E-10
14	4.710E-11	5.603E-11	6.091E-11	6.355E-11	6.493E-11	6.562E-11

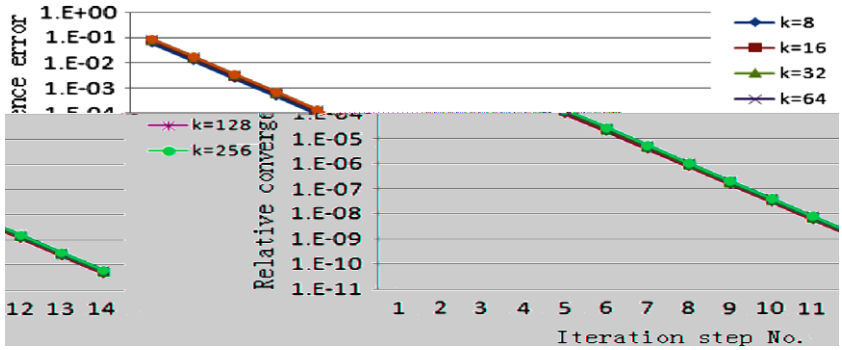

Fig. 7.2. Same convergence history of Dirichlet–Neumann alternating iteration with decreasing maximum mesh size $h = \frac{l_{\mathrm{PEFC}}}{k}$.

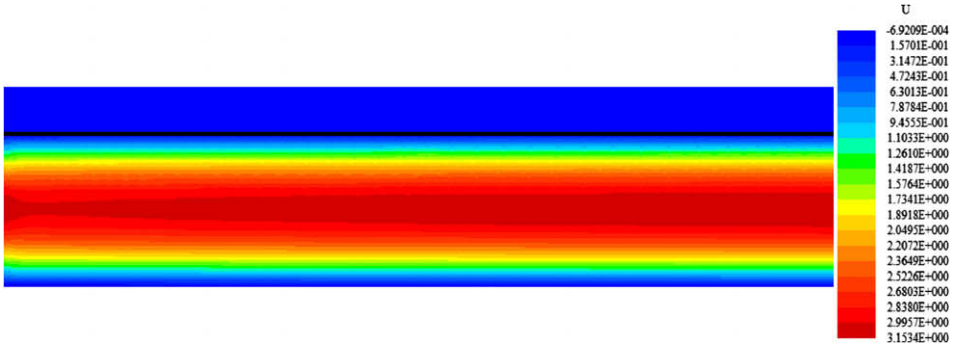

Fig. 7.3. Horizontal two-phase mixture velocity when $C_{\mathrm{in}} = 14\ \mathrm{mol/m^3}$, $u_{\mathrm{in}} = 2\ \mathrm{m/s}$, $I = 1.5\ \mathrm{A\ cm^{-2}}$.

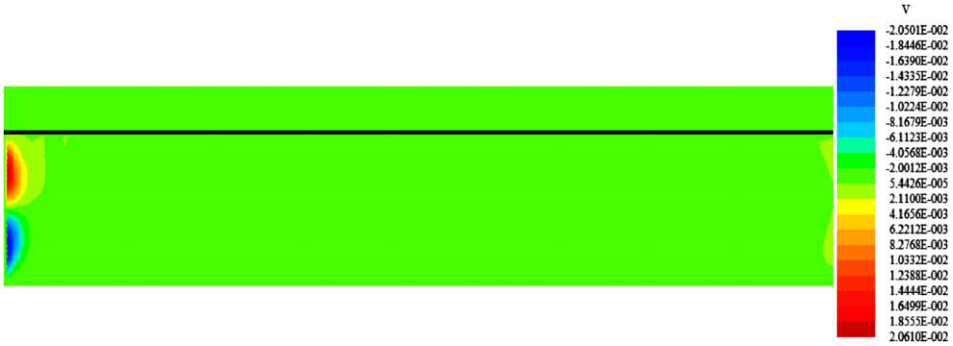

Fig. 7.4. Vertical two-phase mixture velocity when $C_{\mathrm{in}} = 14\ \mathrm{mol/m^3}$,$u_{\mathrm{in}} = 2\ \mathrm{m/s}$, $I = 1.5\ \mathrm{A\ cm^{-2}}$.

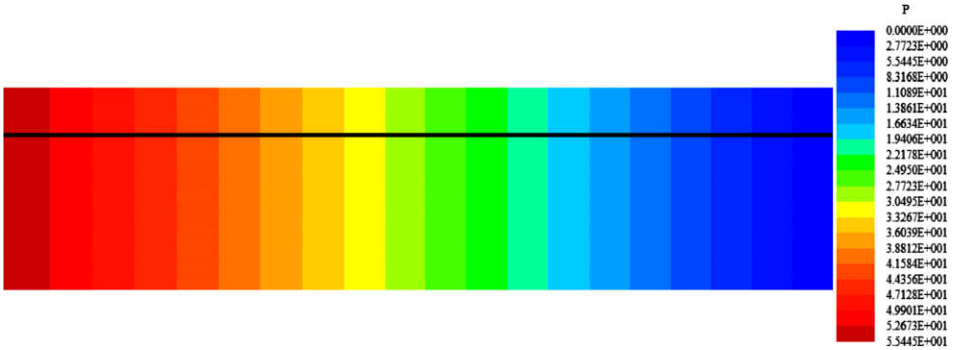

Fig. 7.5. Pressure when $C_{\mathrm{in}} = 14\ \mathrm{mol/m^3}$,$u_{\mathrm{in}} = 2\ \mathrm{m/s}$, $I = 1.5\ \mathrm{A\ cm^{-2}}$.

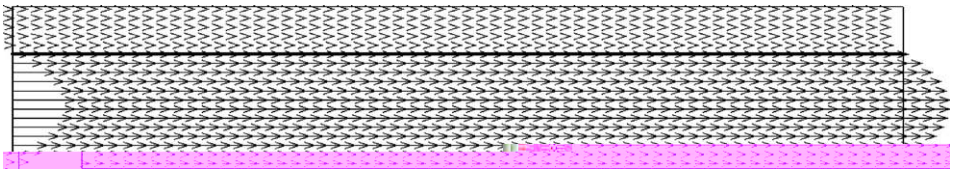

Fig. 7.6. Two-phase mixture velocity field when $C_{in} = 14\ mol/m^3$, $u_{in} = 2\ m/s$, $I = 1.5\ A\ cm^{-2}$.

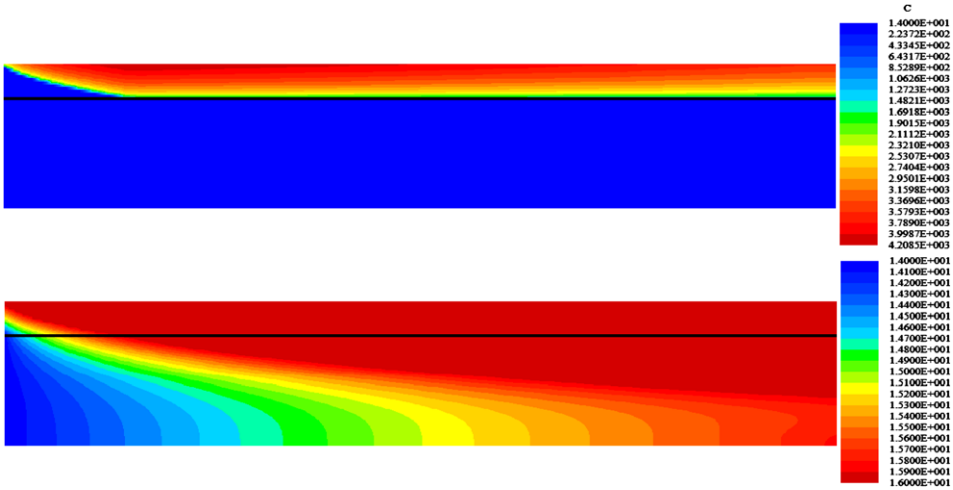

Fig. 7.7. Concentrations of entire water (top) and water vapor (bottom) when $C_{in} = 14\ mol/m^3$, $u_{in} = 2\ m/s$, $I = 1.5\ A\ cm^{-2}$.

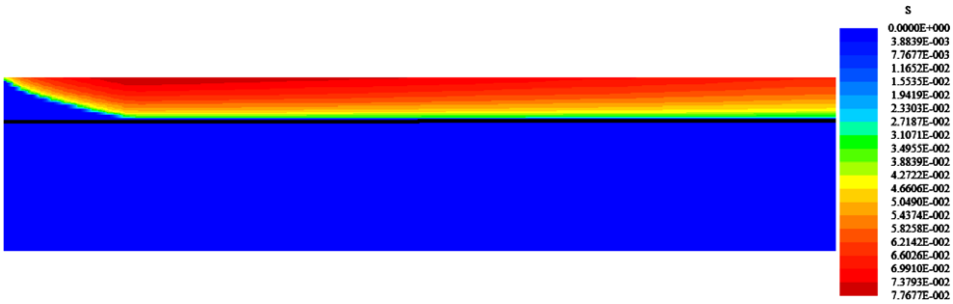

Fig. 7.8. Liquid water-saturation when $C_{in} = 14\ mol/m^3$, $u_{in} = 2\ m/s$, $I = 1.5\ A\ cm^{-2}$. The evaporation front separating the two-phase zone from the single-phase region is approximately represented by $s = 0.03$.

spread to result in a wet channel, as can be seen at the top of Fig. 7.7, where the liquid water, signaled by the water concentration greater than C_{sat}, occupies the most of the GDL/channel interface near the outlet.

In accordance with Fig. 7.7, liquid water is seen in the most upper-right part of Fig. 7.8 to coexist with the saturated water vapor. The largest liquid amount predicted in Fig. 7.8 is around 7.8% at the average current density of $1.5\ A\ cm^{-2}$.

Mass balance error In order to verify the correctness of our numerical solutions, we compute the error of mass balance between the inlet and outlet.

First of all, we derive the mass balance equation based on the water concentration Eq. (2.5) for the gas channel. By integrating both sides of (2.5b) over the entire domain, we get

$$-\int_{\partial\Omega} D_g^{eff} \frac{\partial C}{\partial n} d\tau + \int_{\partial\Omega} C\vec{u} \cdot \vec{n}\, d\tau = 0 \tag{7.1}$$

where $\vec{n}$ denotes the outer normal vector, $\frac{\partial C}{\partial n}$ represents the normal derivative of concentration C, and τ is the arc length coordinate on the boundary. By substituting boundary conditions assigned in Section 2.3 and (6.9) for the boundary integrals in (7.1) and applying (2.11), we get the following approximate mass balance equation:

$$\int_{\partial\Omega_{\text{outlet}}} Cu_x d\tau - \int_{\partial\Omega_{\text{inlet}}} C_{\text{in}} u_x|_{\text{inlet}} d\tau = \int_0^{\text{PEFC}} \frac{I(\tau)}{2F} d\tau = \frac{I_1 + I_2}{4F} l_{\text{PEFC}}, \tag{7.2}$$

where we drop the normal diffusional flux $\int_{\partial\Omega_{\text{inlet}}} D_g^{\text{eff}} \frac{\partial C}{\partial n} d\tau$ at the inlet by simply assuming $\frac{\partial C}{\partial n} \approx 0$ therein. In fact, $\frac{\partial C}{\partial n} = 0$ is physically true at channel inlet in the respect that, in practice, the input gas has been well developed in external pipe before it arrives at the channel inlet of the fuel cell. We provide *Dirichlet* boundary condition $C = C_{\text{in}}$ instead of $\frac{\partial C}{\partial n} = 0$ at channel inlet based on the consideration of the uniqueness of numerical solution. Otherwise the unique solution of water concentration does not exist because the homogeneous *Neumann* boundary condition is everywhere on $\partial\Omega$. On the other hand, since the large gradient of concentration always occurs in the places that are far away from the inlet, in the sense of numerical approximation, $\frac{\partial C}{\partial n}$ indeed practically vanishes at the channel inlet.

Mass balance Eq. (7.2) indicates that the net incremental mass equals the outcome due to the source term, here it is the resultant of electrochemical reaction occurring at the membrane/cathode surface. Consequently the relative error of mass balance is defined as follows:

$$\text{mass balance error} = \frac{\left| \int_{\partial\Omega_{\text{outlet}}} Cu_x d\tau - \int_{\partial\Omega_{\text{inlet}}} C_{\text{in}} u_x|_{\text{inlet}} d\tau - \frac{I_1+I_2}{4F} l_{\text{PEFC}} \right|}{\int_{\partial\Omega_{\text{inlet}}} C_{\text{in}} u_x|_{\text{inlet}} d\tau} \tag{7.3}$$

By inserting the computed concentration C and velocity u_x into (7.3), and computing those integrals in terms of one simple numerical quadrature, say, trapezoidal quadrature rule, we attain a convergent mass balance error from the numerical solutions along with decreasing dimidiate mesh size h, as shown in Table 7.2.

Table 7.2 numerically reveals that the convergent mass balance error is decreasing along with the decreasing mesh size h, and the same result is also obtained in Case 2.

Case 2: C_{in} = 14 mol/m^3, u_{in} = 2 m/s, average current density I = 2 A cm^{-2} Keep the same entry concentration and velocity as Case 1, we increase the average current density to 2 A cm^{-2} in this case by assigning I_1 = 25,000 A/m^2 and I_2 = 15,000 A/m^2. In this case, more water is produced at the membrane/cathode surface and liquid water is expected to appear in the gas channel, namely a wet channel case. By numerically simulating this case within only 11 outer iteration steps in Algorithm A2, and up to 10 inner *Dirichlet–Neumann* alternating iteration steps in Algorithm A1, we attain reasonable numerical solutions that supports our expectation, as shown in Fig. 7.9. Comparing with Fig. 7.7 in Case 1, the two-phase region in Fig. 7.9 is extended further towards the inlet of the gas channel, implying that more liquid water accumulates in the gas channel.

The mass balance error of numerical solutions holds the convergence with decreasing mesh size h, as shown in Table 7.3, together with fast convergence of the numerical iteration, indicating again the good accuracy of this case Similarly, *Dirichlet–Neumann* alternating iteration still holds uniform convergence within 10 inner iteration steps in the first outer iteration step, along with deceasing dimidiate mesh size h. We omit the corresponding table and diagram of convergence history here.

Table 7.2
Convergent mass balance error for the case of C_{in} = 14 mol/m^3, u_{in} = 2 m/s, I = 1.5 A cm^{-2}

Mesh size (h)	Mass balance error
$7. \times 10^{-3}$	1.165×10^{-1}
3.5×10^{-3}	8.411×10^{-2}
1.75×10^{-3}	3.353×10^{-2}

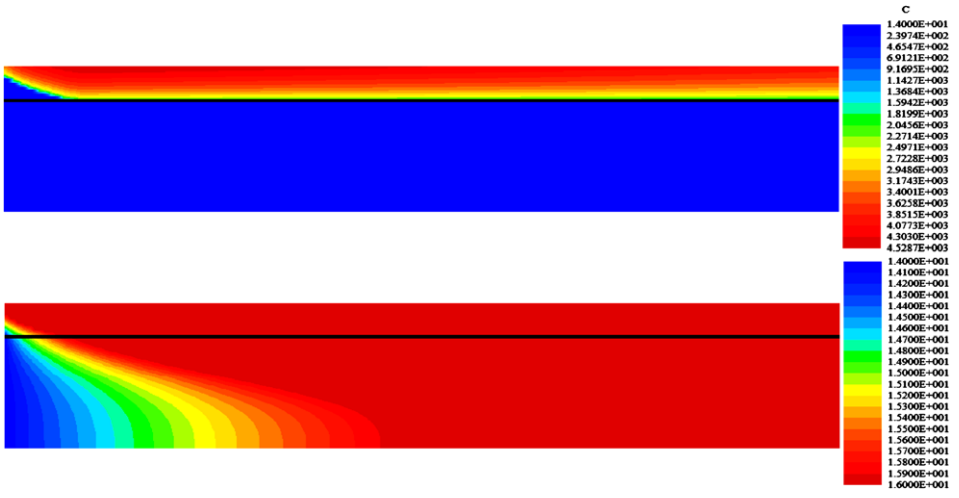

Fig. 7.9. Concentrations of entire water (top) and water vapor (bottom) when C_{in} = 14 mol/m^3, u_{in} = 2 m/s, I = 2 A ;cm^{-2}.

Table 7.3
Convergent mass balance error for the case of C_{in} = 14 mol/m^3, u_{in} = 2 m/s, I = 2 A cm^{-2}

Mesh size (h)	Mass balance error
$7. \times 10^{-3}$	1.257×10^{-1}
3.5×10^{-3}	6.414×10^{-2}
1.75×10^{-3}	1.151×10^{-2}

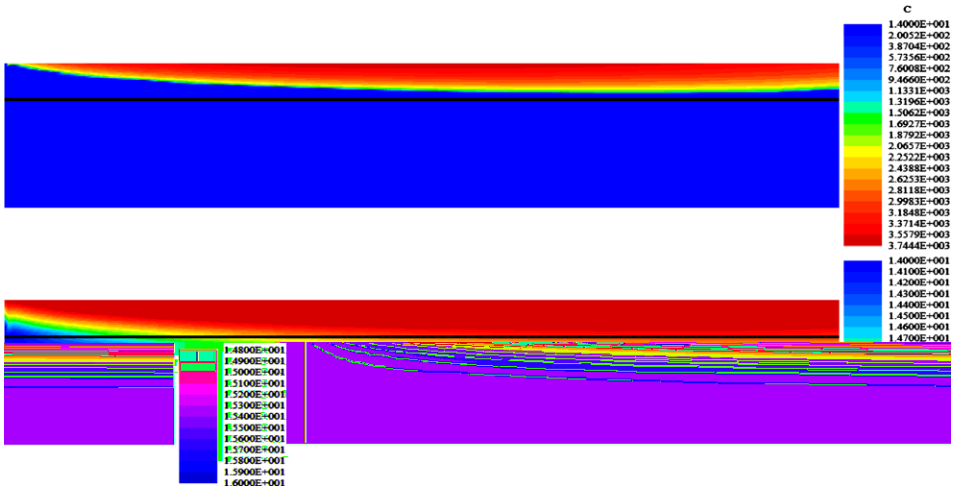

Fig. 7.10. Concentrations of entire water (top) and water vapor (bottom) when C_{in} = 14 mol/m^3,u_{in} = 3 m/s, I = 1.5 A cm^{-2}.

Table 7.4
Mass balance error for the case of C_{in} = 14 mol/m^3, u_{in} = 3 m/s, I = 1.5 A cm^{-2} with mesh size $h = 3.5 \times 10^{-3}$

Outlet flux	F_{out}	4.4996×10^{-2} mol/m·s
Inlet flux	F_{in}	4.1962×10^{-2} mol/m·s
Source	S	5.4411×10^{-3} mol/m·s
Mass balance error	$\frac{\lvert F_{out} - F_{in} - S \rvert}{F_{in}}$	5.7364×10^{-2}

Case 3: C_{in} = 14 mol/m^3,u_{in} = 3 m/s, average current density I = 1.5 A cm^{-2} We intend to build a dry gas channel in this case by using a larger inlet velocity than Case 1. The numerical methods is obtained within 11 outer nonlinear iteration steps in Algorithm A2, and up to 10 inner *Dirichlet–Neumann* alternating iteration steps in Algorithm A1.

The contours of water concentration are typically illustrated in Fig. 7.10, where the water concentration below C_{sat}, indicative of the gas phase only, occupies the entire gas channel and a big part of the porous GDL. The interface between the two-phase zone and single-phase region is confined inside the GDL, giving rise to a dry channel, as shown in Fig. 7.10.

We also attain a relatively accurate mass balance error for the gained numerical solutions in this case of dry gas channel, as shown in Table 7.4.

8. Conclusions

Numerical experiments indicate that the oscillating nonconvergent nonlinear iteration is a common problem in the numerical simulation of two-phase transport for the cathode of a polymer electrolyte fuel cell. We have found that the discontinuous and degenerate diffusivity in the water concentration equation and the dominant convection coefficients in the gas channel are two crucial reasons to prevent the entire nonlinear iteration from convergence.

We demonstrate that *Kirchhoff* transformation is effective in solving the water concentration equation with a discontinuous and degenerate diffusivity. It is a key component of the efficient and stable numerical methodology developed here. Further, an efficient *Newton*'s method is introduced to treat the important inverse *Kirchhoff* transformation. This method significantly decreases the number of iteration and saves the computational cost for the simulation of two-phase water transport.

To handle the case of a wet gas channel, we introduce a domain decomposition method, *Dirichlet–Neumann* alternating iteration, to solve the reformulated water concentration with *Kirchhoff* transformation, which also works equally well for a

dry gas channel. Numerical experiments suggest that our numerical technique efficiently solves the problem of discontinuous solutions across the GDL/channel interface. These arise in the case of a wet channel due to the application of *Kirchhoff* transformation, and eventually produces fast and convergent nonlinear iteration as well as accurate numerical solutions, as compared to oscillating iterations with standard finite element or finite volume methods without Kirchhoff transformation.

In addition, in our decoupled *Picard*'s linearization for *Navier–Stokes* equations and *Dirichlet–Neumann* alternating iteration for the water concentration equation, in order to automatically control dominant convection coefficients in the gas channel, we employ combined mixed and standard finite element-upwind finite volume method for momentum and water concentration equations, respectively. This method does not require any stabilization parameter and play a critical role in attaining fast iteration as well as stable and accurate solutions.

Acknowledgments

This work was supported in part by NSF DMS-0609727 and by the Center for Computational Mathematics and Applications of Penn State. Pengtao Sun was also supported in part by Research Development Award of University of Nevada Las Vegas. Jinchao Xu was supported in part by NSFC-10501001 and Alexander H. Humboldt Foundation. We thank anonymous referee for his/her valuable suggestions to improve the paper.

References

[1] H. Alt, S. Luckhaus, Quasilinear elliptic–parabolic differential equations, Math. Z. 183 (1983) 311–341.
[2] T. Arbogast, M. Wheeler, N. Zhang, A nonlinear mixed finite element method for a degenerate parabolic equation arising in flow in porous media, SIAM J. Numer. Anal. 33 (1996) 1669–1687.
[3] D.N. Arnold, Mixed finite element methods for elliptic problems, Comput. Meth. Appl. Mech. Eng. 82 (1990) 281–300.
[4] J. Bear, Dynamics of Fluids in Porous Media, Elsevier, New York, 1972.
[5] G. Beavers, D. Joseph, Boundary conditions at a naturally impermeable wall, J. Fluid Mech. 30 (1967) 197–207.
[6] H. Berninger, R. Kornhuber, O. Sander, On nonlinear Dirichlet–Neumann algorithms for jumping nonlinearities, Lecture Notes Comput. Sci. Eng. 55 (2007) 491–498.
[7] J. Crank, Free and Moving Boundary Problems, Clarendon Press, 1984.
[8] R.E. Ewing, O.P. Iliev, R.D. Lazarov, Numerical simulation of contamination transport due to flow in liquid and porous media, Technical Report 1992-10, Enhanced Oil Recovery Institute, University of Wyoming, 1992.
[9] N. Eyres, D. Hartree, J. Ingham, R. Jackson, R. Sarjant, S. Wagstaff, The calculation of variable heat flow in solids, Philos. Trans. Roy. Soc. London A240 (1946) 1–57.
[10] Y. Fan, R. Tanner, N. Phan-Thien, Galerkin/least-square finite-element methods for steady viscoelastic flows, J. Non-Newtonian Fluid Mech. 84 (1999) 233–256.
[11] M. Feistauer, J. Felcman, On the convergence of a combined finite volume-finite element for nonlinear convection–diffusion problems, Numer. Meth. Partial Differen. Equat. 13 (1997) 163–190.
[12] M. Feistauer, J. Felcman, M. Lukáčová-Medvid'ová, Combined finite element-finite volume solution of compressible flow, J. Comput. Appl. Math. 63 (1995) 179–199.
[13] M. Feistauer, J. Slavik, P. Stupka, On the convergence of a combined finite volume-finite element methods for nonlinear convection–diffusion problems. Explicit schemes, Numer. Meth. Partial Differen. Equat. 15 (1999) 215–235.
[14] L. Franca, T. Hughes, Convergence analyses of Galerkin least-square methods for symmetric advective-diffusive forms of the stokes and incompressible Navier–Stokes equations, Comput. Meth. Appl. Mech. Eng. 105 (1993) 285–298.
[15] W. Jäger, A. Mikelić, On the interface boundary condition of Beavers, Joseph, and Saffman, SIAM J. Appl. Math. 60 (2000) 1111–1127.
[16] C. Johnson, A.H. Schatz, L.B. Wahlbin, Crosswind smear and pointwise errors in streamline diffusion finite element methods, Math. Comput. 49 (1987) 25–38.
[17] T. Kang, D. Yu, Some a posteriori error estimates of the finite-difference streamline-diffusion method for convection-dominated diffusion equations, Adv. Comput. Math. 15 (2001) 193–218.
[18] N. Kladias, V. Prasad, Experimental verification of Darcy–Brinkman–Forchheimer flow model for natural convection in porous media, J. Thermophys. Heat Trans. 5 (1991) 560–576.
[19] D. Kroner, S. Noelle, M. Rokyta, Convergence of higher order upwind finite volume schemes on unstructured grids for scalar conservation laws in several space dimensions, Numer. Math. 71 (1995) 527–560.
[20] D. Kröner, M. Ohlberger, A posteriori error estimates for upwind finite volume schemes for nonlinear conservation laws in multi-dimensions, Math. Comput. 69 (2000) 25–39.
[21] D. Kroner, M. Rokyta, Convergence of upwind finite volume schemes for scalar conservation laws in two-dimensions, SIAM J. Numer. Anal. 31 (1994) 324–343.
[22] J.-H. Nam, M. Kaviany, Effective diffusivity and water-saturation distribution in single- and two-layer pemfc diffusion medium, Int. J. Heat Mass Trans. 46 (2003) 4595–4611.
[23] K. Niijima, Pointwise error estimates for a streamline diffusion finite element scheme, Numer. Math. 56 (1990) 707–719.
[24] U. Pasaogullari, C.Y. Wang, Liquid water transport in gas diffusion layer of polymer electrolyte fuel cells, J. Electrochem. Soc. 151 (2004) A399–A406.
[25] U. Pasaogullari, C.Y. Wang, Two-phase modeling and flooding prediction of polymer electrolyte fuel cells, J. Electrochem. Soc 152 (2005) A380–A390.
[26] A. Quarteroni, A. Valli, Numerical Approximation of Partial Differential Equations, vol. 23, Springer Series in Computational Mathematics, 1997.
[27] A. Quarteroni, A. Valli, Domain Decomposition Methods for Partial Differential Equations, Oxford Science Publications, 1999.
[28] H.G. Roos, H. Zarin, The streamline-diffusion method for a convection–diffusion problem with a point source, J. Comput. Appl. Math. 150 (2003) 109–128.
[29] M. Rose, Numerical methods for flows through porous media. I, Math. Comput. 40 (1983) 435–467.
[30] P. Saffman, On the boundary condition at the surface of a porous media, Stud. Appl. Math. 50 (1971) 292–315.
[31] A. Scheidegger, The Physics of Flow Through Porous Media, University of Toronto Press, Toronto, 1958.
[32] T. Springer, T. Zawodzinski, S. Gottesfeld, Polymer electrolyte fuel cell model, J. Electrochem. Soc. 138 (1991) 2334–2342.
[33] T.E. Springer, M.S. Wilson, S. Gottesfeld, Modeling and experimental diagnostics in polymer electrolyte fuel cells, J. Electrochem. Soc. 140 (1993) 3513–3526.
[34] M. Stynes, L. Tobiska, The SDFEM for a convection–diffusion problem with a boundary layer: optimal error analysis and enhancement of accuracy, SIAM J. Numer. Anal. 41 (2003) 1620–1642.
[35] P. Sun, R. Russell, J. Xu, A new adaptive local mesh refinement algorithm and its application on fourth order thin film flow problem, J. Comput. Phys. 224 (2007) 1021–1048.

[36] P. Sun, J. Xu, Research Notes of Numerical Simulation on Two-phase Steady-state Transport Model in pefc Cathode, Technical Report AM318, Computational and Applied Mathematics, Pennsylvania State University, 2007.
[37] P. Sun, G. Xue, C. Wang, J. Xu, Fast numerical simulation of two-phase transport model in the cathode of polymer electrolyte fuel cell, Commun. Comput. Phys. 6 (2009) 49–71.
[38] T.E. Tezduyar, Stabilized finite element formulations for incompressible flow computations, Adv. Appl. Mech. 28 (1992) 1–44.
[39] L. Thompson, P. Pinsky, A Galerkin least-squares finite element method for the two-dimensional Helmholtz equation, Int. J. Numer. Meth. Eng. 38 (1994) 371–397.
[40] V. Voller, Numerical treatment of rapidly changing and discontinuous conductivities, Technical Note, Int. J. Heat Mass Trans. 44 (2001) 4553–4556.
[41] V. Voller, C. Swaminathan, Treatment of discontinuous thermal conductivity in control-volume solutions phase-change problems, Numer. Heat Trans. 24B (1993) 161–180.
[42] C.Y. Wang, Fundamental models for fuel cell engineering, Chem. Rev. 104 (2004) 4727–4766.
[43] C.Y. Wang, P. Cheng, Multiphase flow and heat transfer in porous media, Adv. Heat Trans. 30 (1997) 93–196.
[44] C.Y. Wang, Z.H. Wang, Y. Pan, Two-phase transport in proton exchange membrane fuel cells, in: Proceedings of the International Mechanical Engineering, Congress & Exhibits, Nashville, TN, 1999.
[45] Z. Wang, C.Y. Wang, K.S. Chen, Two-phase flow and transport in the air cathode of proton exchange membrane fuel cells, J. Power Sources 94 (2001) 40–50.
[46] C. Woodward, C. Dawson, Analysis of Expanded Mixed Finite Element Methods for a Nonlinear Parabolic Equation Modeling Flow into Variably Saturated Porous Media, Texas Inst. Comp. Appl. Math. University of Texas at Austin, TIACM Report 96-51, 1996.
[47] X. Xie, J. Xu, G. Xue, Uniformly stable finite element methods for Darcy–Stokes–Brinkman models, J. Comput. Math. 26 (2008) 437–455.